or at 60 min after insulin infusion (Figures S3C and S3D). Moreover, there were no significant differences in the results of the insulin tolerance or glucose tolerance tests, or in the skeletal muscle glucose uptake among the three groups (Figures S3E–S3G). These data strongly suggest that the effects of both BPS and $_L$-NAME were eNOS dependent. The GIR and Rd were completely restored in the BPS-treated ETIrs2KO mice at 60 and 120 min after insulin infusion (Figure 4F and data not shown). We also measured the glucose uptake by the skeletal muscle after insulin infusion in the hyperinsulinemic-euglycemic clamp study. Glucose uptake by the skeletal muscle after insulin infusion was completely restored in the BPS-treated ETIrs2KO mice (Figure 4G). On the other hand, the glucose uptake by the isolated skeletal muscle from the BPS-treated ETIrs2KO mice remained essentially unchanged (Figure 4H), indicating the absence of any significant effect of BPS treatment on the glucose uptake by the skeletal muscle per se. Consistent with the results for the interstitial insulin concentrations, the phosphorylation levels of Irβ, as well as those of Irs1 and Akt, in the skeletal muscle were also completely restored in the BPS-treated ETIrs2KO mice at 60 min after insulin infusion into the inferior vena cava (Figure S3H). These data suggest that restoration of the insulin-induced phosphorylation of eNOS in the endothelial cells also restored the insulin-induced capillary recruitment and increase of the interstitial concentrations of insulin, consequently restoring the insulin-induced glucose uptake by the skeletal muscle. Alternatively, there is also the possibility that concomitant BPS plus insulin treatment activated eNOS via a pathway independent of the insulin/Irs/Akt pathway, even though BPS alone had no effect on eNOS phosphorylation. No significant differences were observed in the food intake, body weight, or weights of the visceral and subcutaneous fat pads among the three groups (Figure S4A). No significant differences in the plasma lipid profile or expression levels of adipokines were observed either among the three groups (Figures S4B and S4C). No significant difference in the 2-[^{3}H]DG uptake by the skeletal muscle was noted between the saline- and $_L$-NAME-treated control mice (Figure S4D).

Restoration of Insulin-Induced eNOS Phosphorylation in the Endothelial Cells Restored the Glucose Uptake by the Skeletal Muscle in the HF Diet-Fed Mice

Could the restoration of insulin-induced eNOS phosphorylation in the endothelial cells also ameliorate the impaired glucose uptake by the skeletal muscle in the HF diet-fed obese mice? BPS treatment significantly increased the eNOS mRNA (Figure 5A) and protein (Figure 5B) expression levels. BPS treatment in the HF diet-fed mice restored insulin-induced phosphorylation of eNOS to a level similar to that observed in the saline-treated

normal chow-fed mice (Figure 5B), despite the absence of any change in the ratio of phosphorylated eNOS to total eNOS in the BPS-treated HF diet-fed mice (Figure 5B); also, no change in the insulin-induced phosphorylation of Akt was observed in these mice (Figure S5A). These data suggest that restoration of the insulin-induced eNOS phosphorylation in the BPS-treated HF diet-fed mice was not due to improvement of insulin signaling, but was rather proportional to the protein expression levels of eNOS. The decreased capillary blood volume and interstitial concentrations of insulin observed in the saline-treated HF diet-fed mice were restored at 60 and 120 min after insulin infusion in the BPS-treated HF diet-fed mice (Figures 5C and 5D and data not shown), when the plasma insulin levels were adjusted to be the same among the three groups (Figure S5B and data not shown). The restoration of the capillary blood volume by BPS treatment at 60 min after insulin infusion in the HF diet-fed mice was completely blocked by $_L$-NAME treatment (Figure 5E). Consequently, the GIR and Rd at 60 and 120 min after insulin infusion were significantly, but not completely, restored by BPS treatment, although the increased EGP remained unchanged (Figure 5F and data not shown). We also measured the skeletal muscle glucose uptake after insulin infusion in the hyperinsulinemic-euglycemic clamp study. Glucose uptake by the skeletal muscle after insulin infusion was significantly, but not completely, restored in the BPS-treated HF diet-fed mice (Figure 5G). On the other hand, the glucose uptake by isolated skeletal muscle from the HF diet-fed mice treated with BPS remained essentially unchanged (Figure 5H), indicating the absence of any significant effect of BPS treatment on the glucose uptake by the skeletal muscle per se. Consistent with the results for the interstitial insulin concentrations, the insulin-induced phosphorylation levels of Irβ, as well as those of Irs1 and Akt, in the skeletal muscle at 60 min after insulin infusion into the inferior vena cava were significantly, but not completely, restored in the BPS-treated HF diet-fed mice (Figure S5C). Moreover, the increase in the blood glucose after glucose loading was significantly, but not completely, ameliorated during an oral glucose tolerance test conducted after BPS treatment in the HF diet-fed mice (Figure S5D). No significant differences in the food intake, body weight, or weights of the visceral and subcutaneous fat pads were noted between the saline- and BPS-treated HF diet-fed mice (Figure S5E). No significant differences in the plasma lipid profile or expression levels adipokines were noted between the saline- and BPS-treated HF diet-fed mice (Figures S5F and S5G). Taken together, restoration of insulin-induced eNOS activation in the endothelial cells restored the insulin-induced capillary recruitment and interstitial insulin concentrations, resulting in improvement of the skeletal muscle glucose uptake in the HF diet-fed obese mice.

(C) Insulin-stimulated phosphorylation levels of Akt and eNOS in the endothelial cells of the ETIrs1KO mice (n = 3–5).

(D and E) Insulin tolerance test (D) and glucose tolerance test (E) in the ETIrs1KO mice (n = 6).

(F) GIR, EGP, and Rd in the ETIrs1KO mice during the hyperinsulinemic-euglycemic clamp study (n = 6–8).

(G and H) Expression levels of Irs1, Irs2, eNOS, and ET-1 mRNA and protein in the endothelial cells of the ETIrs1/2DKO mice (n = 3–6).

(I) Insulin-stimulated phosphorylation levels of Akt and eNOS in the endothelial cells of the ETIrs1/2DKO mice (n = 5–6).

(J and K) Insulin tolerance test (J) and glucose tolerance test (K) in the ETIrs1/2DKO mice (n = 8–9).

(L) GIR, EGP, and Rd in the ETIrs1/2DKO mice during the hyperinsulinemic-euglycemic clamp study (n = 5–10). "Control" of ETIrs1KO mice indicates Irs1$^{lox/lox}$ mice; "Control" ETIrs1/2DKO mice indicates Irs1$^{lox/lox}$/Irs2$^{lox/lox}$ mice. Where error bars are shown, the results represent the means ± SEM. *p < 0.05, **p < 0.01, ***p < 0.001.
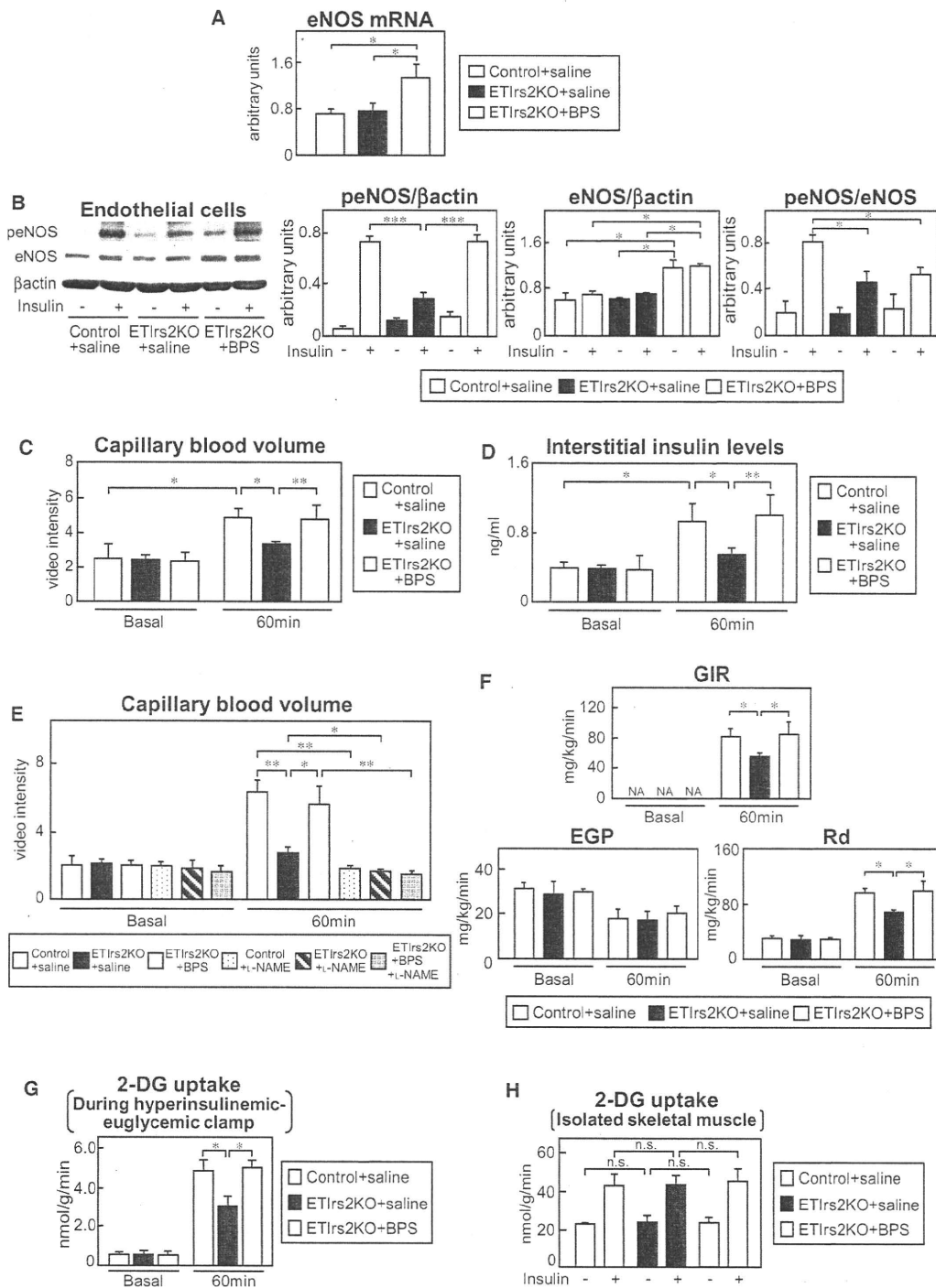
Figure 4. Restoration of the Insulin-Induced Phosphorylation of eNOS in the Endothelial Cells Restored the Insulin-Induced Increase of the Capillary Blood Volume and Interstitial Concentrations of Insulin; as a Consequence, the Insulin-Induced Glucose Uptake by the Skeletal Muscle Was Also Restored in the ETIrs2KO Mice

(A–D) eNOS mRNA levels (A), insulin-stimulated phosphorylation level of eNOS (B), capillary blood volume (C), and interstitial insulin concentrations (D) in the BPS-treated ETIrs2KO mice (n = 5–8).

(E) Capillary blood volume in the BPS-treated ETIrs2KO mice following L-NAME treatment (n = 4–6).

DISCUSSION

In this study, we demonstrated that endothelial insulin signaling is also significantly impaired in HF diet-fed mice, as in the other target organs of insulin, such as the liver and skeletal muscle. Moreover, insulin-induced capillary recruitment, increase of interstitial insulin concentrations, and glucose uptake were also significantly decreased in the skeletal muscle, all of which were reversed by restoration of the insulin-induced phospholyration of eNOS in the endothelial cells. These data suggest that impaired insulin signaling in the endothelial cells, with reduction of Irs2 expression and insulin-induced eNOS phosphorylation, reduces insulin-induced glucose uptake by the skeletal muscle via, at least in part, decreased capillary recruitment and decreased interstitial insulin concentrations in the skeletal muscle. In fact, an insulin signaling defect induced by Irs2 deletion from the endothelial cells caused impaired insulin-induced glucose uptake by the skeletal muscle, along with attenuation of the insulin-induced capillary recruitment and increase of interstitial insulin concentrations.

Based on these data, we provide insight into the mechanism of insulin resistance in the skeletal muscle (Figure 6). Since the plasma insulin levels of lean subjects are low, and the expression levels of Irs2 in their endothelial cells are presumably maintained under the fasting condition, insulin-mediated Akt and eNOS activations are induced optimally after feeding, resulting in insulin-induced capillary recruitment, increase of interstitial insulin concentrations, and increase of glucose uptake by the skeletal muscle. By contrast, since downregulation of Irs2 expression is probably induced by hyperinsulinemia in the endothelial cells of obese subjects, the insulin-mediated Akt and eNOS activations after feeding are inadequate, and as a result, insulin-induced capillary recruitment, increase of interstitial insulin concentrations, and increase of glucose uptake by the skeletal muscle are impaired in obese subjects. This insight into the mechanism also sheds light on the physiological roles of Irs2 in the endothelial cells. Expression of a sufficient amount of Irs2 in the endothelial cells appears to be critical to normal glucose homeostasis. When Irs2 expression is abundant in the fasting state, adequate glucose uptake by the skeletal muscle is induced and the elevated glucose levels return to within the normal range after feeding. However, when Irs2 expression in the endothelial cells is reduced in the fasting state in the presence of hyperinsulinemia with insulin resistance, insulin signaling is impaired, and the elevated glucose levels after feeding fail to decrease efficiently, and in fact, the ETIrs2KO mice actually exhibited glucose intolerance in the glucose tolerance test (Figure 2H).

Insulin normally induces both vasorelaxation and vasoconstriction: insulin-induced vasorelaxation is mediated by the Irs-PI3K-Akt pathway increasing endothelial NO production, and insulin-induced vasoconstriction is mainly mediated by the Shc/SOS/Ras-MAPK pathway inducing ET-1 expression

(Muniyappa and Quon, 2007). While insulin-induced eNOS activation was significantly decreased in the endothelial cells of both the ETIrs2KO and ETIrs1/2DKO mice (Figures 2D and 3I), the ET-1 expressions remained unchanged in both models in this study, indicating that insulin signaling was selectively impaired in the endothelial cells of these mice (Figures 3G and 3H; Figures S2A and S2B). This selective insulin signaling defect appears to be critical to the impairment of the insulin-induced glucose uptake by the skeletal muscle. In fact, endothelial-cell-specific insulin receptor-knockout (VENIRKO) mice, in which both the Irs-PI3K-Akt-eNOS and Shc/SOS/Ras-MAPK-ET-1 pathways are disrupted, do not exhibit skeletal muscle insulin resistance (Vicent et al., 2003). Moreover, King et al. demonstrated that while the MAPK activity in the microvessels of obese Zucker rats remained unchanged, the Irs1 protein and Irs1-associated PI3kinase activity were modestly reduced, and the Irs2 protein and Irs2-associated PI3kinase activity were reduced even further (Jiang et al., 1999). Furthermore, VENIRKO mice developed insulin resistance when fed either low- or high-salt diets. These data suggest that the Irs-PI3K-Akt pathway may be more susceptible to the adverse effects of conditions such as obesity and dietary salt intake.

ETIrs2KO mice showed glucose intolerance, insulin resistance, and impaired glucose uptake by the skeletal muscle in vivo (Figures 2G–2J), despite the skeletal muscle per se not showing impaired insulin-induced glucose uptake (Figure 2K). In contrast, although myocyte-specific insulin receptor-knockout mice exhibited impaired glucose uptake by the skeletal muscle per se, as glucose uptake by insulin was decreased in the isolated skeletal muscle, the glucose tolerance and insulin sensitivity were almost normal in vivo (Brüning et al., 1998). Why did the ETIrs2KO, but not MIRKO, mice show skeletal muscle insulin resistance in vivo? It has been reported that there are mainly two different pathways of physiological glucose uptake by the skeletal muscle: one mediated in an insulin-dependent manner, such as after a meal, and the other in an insulin-independent manner, such as during exercise (Clark, 2008). Considering the phenotype of the MIRKO mice, the glucose uptake in the myocytes showing defective expression of the insulin receptor throughout growth and development may be largely compensated for by insulin-receptor-independent glucose uptake mechanisms. There may be little such compensatory mechanisms for glucose uptake in the ETIrs2KO mice, which show adequate expression of the insulin receptor in the skeletal muscle. Consequently, these mice may exhibit impairment of insulin-induced glucose uptake by the skeletal muscle, unlike the MIRKO mice.

To what degree is the impaired insulin delivery induced by the endothelial insulin signaling defect involved in the skeletal muscle insulin resistance in obesity and type 2 diabetes? Glucose uptake by the skeletal muscle was restored by 50% or more with improvement of the endothelial insulin signaling and insulin delivery in HF diet-fed mice (Figures 5B and 5G).

(F) GIR, EGP, and Rd in the BPS-treated ETIrs2KO mice after insulin infusion in the hyperinsulinemic-euglycemic clamp study (n = 4–8).

(G) Glucose uptake by the skeletal muscle in the BPS-treated ETIrs2KO mice after insulin infusion in the hyperinsulinemic-euglycemic clamp study (n = 4–8).

(H) Glucose uptake by the isolated skeletal muscle in the BPS-treated ETIrs2KO mice (n = 3–6). "NA" indicates not applicable. Where error bars are shown, the results represent the means ± SEM. *p < 0.05, **p < 0.01, ***p < 0.001.
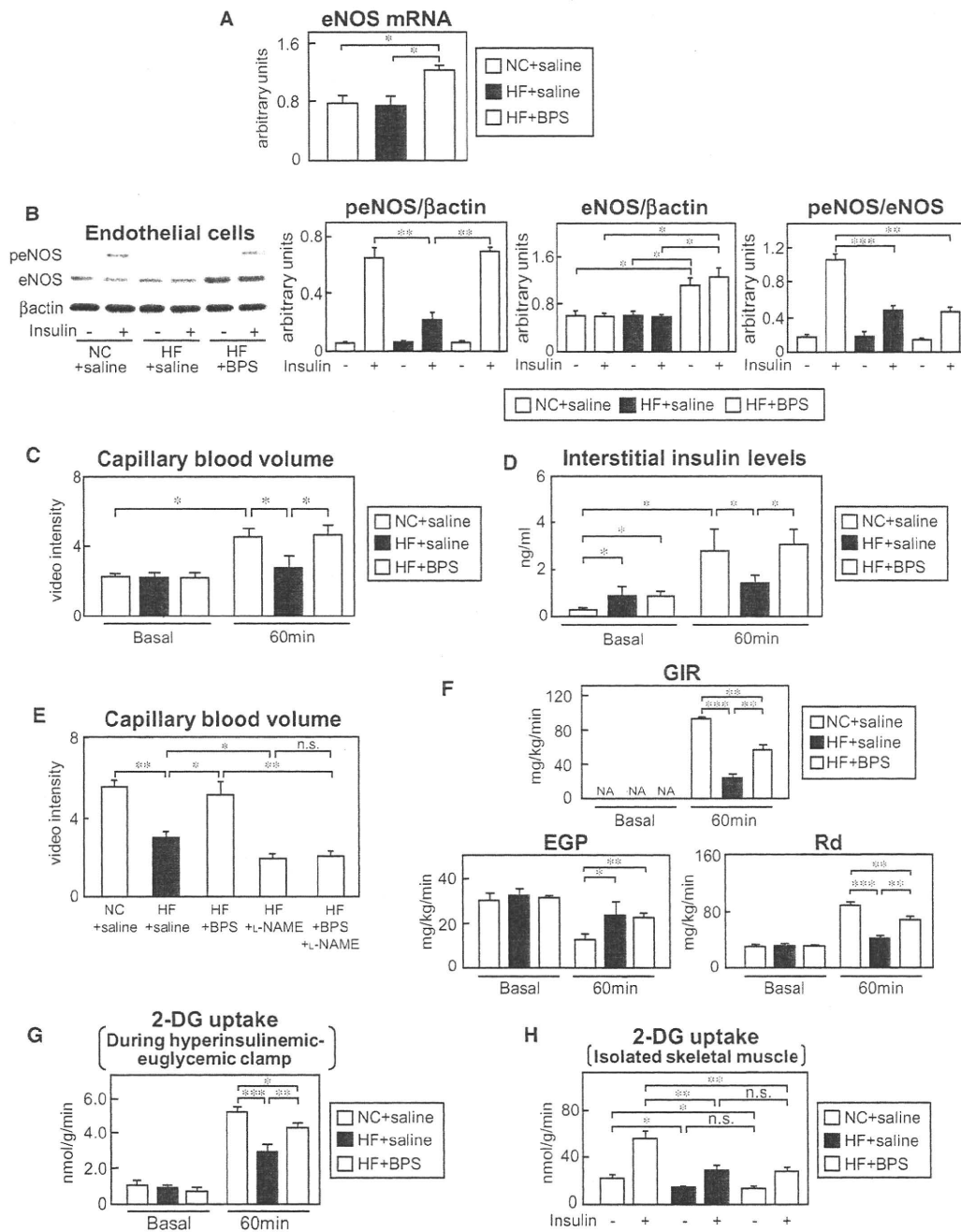
Figure 5. Restoration of the Insulin-Induced Phosphorylation of eNOS Restored the Insulin-Induced Increase of the Capillary Blood Volume and Interstitial Insulin Concentrations, Resulting in Improvement of the Glucose Uptake by the Skeletal Muscle in the HF Diet-Fed Obese Mice

(A–D) eNOS mRNA levels in the endothelial cells (A), insulin-stimulated phosphorylation level of eNOS (B), capillary blood volume (C), and interstitial insulin concentrations (D) in the BPS-treated HF diet-fed mice (n = 5–8).

(E) Capillary blood volume in the BPS-treated HF diet-fed mice following L-NAME treatment (n = 4–6).

(F) GIR, EGP, and Rd in the BPS-treated HF diet-fed mice after insulin infusion in the hyperinsulinemic-euglycemic clamp study (n = 3–5).

(G) Glucose uptake by the skeletal muscle in the BPS-treated HF diet-fed mice after insulin infusion in the hyperinsulinemic-euglycemic clamp study (n = 3–5).

(H) Glucose uptake by the isolated skeletal muscle in the BPS-treated HF diet-fed mice (n = 3–5). "NC" indicates normal chow-fed mice. "NA" indicates not applicable. Where error bars are shown, the results represent the means ± SEM. $*p < 0.05$, $**p < 0.01$, $***p < 0.001$.
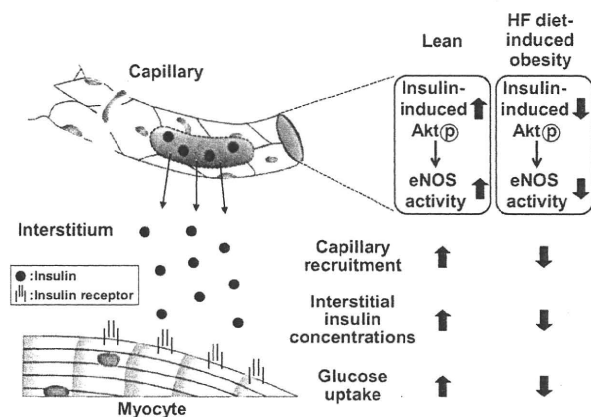
Figure 6. Impaired Insulin Signaling in the Endothelial Cells Reduces Insulin-Induced Glucose Uptake by the Skeletal Muscle in Obese Subjects

In lean subjects, the insulin-mediated Akt and eNOS activations are induced optimally in the endothelial cells after feeding, resulting in insulin-induced capillary recruitment, increase of interstitial insulin concentrations, and increase of the glucose uptake by the skeletal muscle. By contrast, since the insulin-mediated Akt and eNOS activations are inadequate in the endothelial cells of obese subjects after feeding, the insulin-induced capillary recruitment, increase or interstitial insulin concentrations, and increase of glucose uptake by the skeletal muscle are impaired.

Moreover, insulin delivery into the interstitial fluid is known to be delayed in insulin resistance (Sjostrand et al., 2002), as also is the onset of insulin stimulation of glucose uptake (Nolan et al., 1997). In addition, delivery of inulin, a molecule whose molecular weight is similar to that of insulin, to the skeletal muscle was reported to be markedly diminished in diet-induced insulin resistance (Ellmerer et al., 2006). These findings suggest that impairment of insulin delivery, possibly caused by an endothelial insulin signaling defect, may play a critical role in the skeletal muscle insulin resistance seen in obesity.

Why were decreased insulin signaling and decreased glucose uptake in response to insulin observed only in the skeletal muscle of the ETIrs2KO mice and not in their liver? The difference between the types of capillaries in the liver and skeletal muscle may explain these differences in the insulin sensitivity of the two organs. It is thought that the occluded junctions of the endothelial cells of the capillaries in the skeletal muscle may prevent paracellular transport of most macromolecules, including insulin, whereas the fenestrated endothelium of the capillaries in the liver freely permits paracellular passage of macromolecules (Aird, 2007). In fact, more rapid insulin action kinetics have been observed in the liver than in the skeletal muscle (Sherwin et al., 1974).

Insulin-induced phosphorylation of Akt and eNOS in the ETIrs2KO mice was significantly, but not completely, impaired by endothelial Irs2 deficiency (Figure 2D), suggesting the important role of both Irs2 and Irs1 in this signaling in the endothelial cells. In fact, phosphorylation of Akt and eNOS was completely abrogated in the ETIrs1/2DKO mice (Figure 3I). Thus, in the physiological state, it is likely that insulin-stimulated Irs1-mediated Akt activates eNOS in proportion to the amount of eNOS protein available in these mice.

In this study, we found that endothelial insulin signaling mediates insulin-stimulated capillary recruitment and increase of interstitial insulin concentrations and, as a consequence, facilitates glucose uptake by the skeletal muscle. Skeletal muscle insulin resistance may be caused by impaired insulin signaling not only in the myocytes but also in the endothelial cells. Taken together, treatment directed at improving insulin signaling in the endothelial cells as well as myocytes may serve as a therapeutic strategy for ameliorating skeletal muscle insulin resistance.

EXPERIMENTAL PROCEDURES

Mice

ETIrs1KO or ETIrs2KO mice were generated by mating Irs1$^{lox/+}$ or Irs2$^{lox/+}$ female mice (Kubota et al., 2008) with transgenic mice expressing Cre under control of the murine Tie2 promoter (Tie2-Cre mice) (Kisanuki et al., 2001). The Irs1$^{lox/+}$:Tie2-Cre or Irs2$^{lox/+}$:Tie2-Cre male offspring were then crossed with Irs1$^{lox/+}$ or Irs2$^{lox/+}$ female mice to obtain WT (Irs1$^{+/+}$), Tie2-Cre (Irs1$^{+/+}$:Tie2-Cre), control (Irs1$^{lox/lox}$), and ETIrs1KO (Irs1$^{lox/lox}$:Tie2-Cre) mice, or WT (Irs2$^{+/+}$), Tie2-Cre (Irs2$^{+/+}$:Tie2-Cre), control (Irs2$^{lox/lox}$), and ETIrs2KO (Irs2$^{lox/lox}$:Tie2-Cre) mice, respectively. To generate endothelial-specific Irs1/Irs2 double-knockout (ETIrs1/2DKO) mice, Irs1$^{lox/+}$:Tie2-Cre or Irs2$^{lox/+}$:Tie2-Cre male mice were crossed with Irs2$^{lox/+}$ or Irs1$^{lox/+}$ female mice, and the resultant Irs1$^{lox/+}$/Irs2$^{lox/+}$:Tie2-Cre male mice were crossed with Irs1$^{lox/+}$/Irs2$^{lox/+}$ female mice. Irs1$^{lox/lox}$/Irs2$^{lox/lox}$ mice were used as the control for ETIrs1/2DKO mice. Only male littermates were used for this study; we did not use the female Tie2-Cre, Irs1$^{lox/+}$:Tie2-Cre, Irs2$^{lox/+}$:Tie2-Cre, Irs1$^{lox/+}$/Irs2$^{lox/+}$:Tie2-Cre, ETIrs1KO, ETIrs2KO, or ETIrs1/2DKO mice for breeding. Further information is provided in the Supplemental Information. The animal care and experimental procedures used in this study were approved by the Animal Care Committee of the University of Tokyo.

Capillary Blood Volume

The capillary blood volume was measured by contrast-enhanced ultrasound, as described previously (Vincent et al., 2004), with some modifications. The hindlimb muscles were imaged in the short axis using a 40 MHz transducer (RMV 704) connected to an ultrasound system (Vevo 770; VISUALSONICS Inc.). Sonazoid (Daiichi Sankyo Corporation) was infused into the animals, which were divided into three groups for the measurements at 0, 10, and 60 min after the hyperinsulinemic-euglycemic clamp, a high-power ultrasound with a frequency of 1 MHz was applied to the lower leg muscles, and images were collected for 30 s to assess the enhancement. The ultrasound intensity in decibels within the region of interest was converted to the acoustic intensity after background subtraction using 0.5 s ultrasound images, and the microvascular volume, fill rate constant, and capillary blood volume were calculated according to the equation $y = A(1 - e^{-\beta t})$. Further information is provided in the Supplemental Information.

Interstitial Concentrations of Insulin in the Skeletal Muscle

Muscle microdialysis was performed in the hindlimb muscles using a 4 mm microdialysis tubing (CMA-20) at the rate of 0.3 μl/min. We conducted calibration using the no-net flux technique described previously (Jansson et al., 1993), with slight modifications. Briefly, four known concentrations of insulin (0 ng/ml, 0.5 ng/ml, 1 ng/ml, and 1.5 ng/ml) above and below the expected concentration in the skeletal muscle were used. The insulin solutions were added to the perfusate, and the net changes in the concentrations of the analytes in the dialysate were recorded (insulin$_{out}$ − insulin$_{in}$ = net change). Regression analysis yielded a linear relationship between the concentrations in the perfusates and the dialysates. The intercept with the x axis indicates the insulin concentrations in the perfusate at equilibrium with the surrounding medium, and the slope of the line yields the dialysis recovery by the no-net flux technique. The insulin concentrations in the interstitial fluid were calculated from the dialysis recovery by the no-net flux technique and the in vivo dialysate insulin concentration, as described previously (Sjostrand et al., 2002).

Endothelial Cell Culture

The aorta was dissected out from the aortic arch to the abdominal aorta and immersed in 10% FBS-DMEM containing 1000 U/ml heparin. A 24-gauge cannula was inserted into the proximal portion of the aorta. The other side was tied, and the lumen was filled with a solution of collagenase type II (2 mg/ml, dissolved in serum-free DMEM). After incubation at 37°C for 45 min, the endothelial cells were removed from the aorta by flushing with 5 ml of DMEM containing 10% FBS and cultured in a 35 mm collagen type 1-coated dish. Further information is provided in the Supplemental Information.

Hyperinsulinemic-Euglycemic Clamp

An infusion catheter was inserted into the right jugular vein of the mice, as described previously (Kubota et al., 2008), with some modifications. 1% glucose ([6,6-^{2}H$_2$]glucose [Sigma]) was infused intravenously, and after a 90 min basal period a blood sample was collected from the tail tip for determination of the basal glucose specific activity. To measure the GIR, a primed-continuous infusion of insulin (Humulin R; Lilly) was administered and the blood glucose concentration was maintained at approximately 120 mg/dl by the administration of glucose (5 g of glucose/10 ml enriched to about 20% with [6,6-^{2}H$_2$]glucose [Sigma]) for 60 or 120 min. Blood samples (20 μl) were obtained for 15 or 30 min before the end of the hyperinsulinemic-euglycemic clamp. Thereafter, the Rd was calculated according to non-steady-state equations, and the EGP was calculated as the difference between the Rd values and the exogenous GIR. Further information is provided in the Supplemental Information.

Statistical Analysis

Values were expressed as means ± SEM. Student's t test was used for statistical analysis of the differences between two groups, and the statistical significance of differences among multiple groups was determined by ANOVA.

SUPPLEMENTAL INFORMATION

Supplemental Information includes six figures, one movie, Supplemental Experimental Procedures, and Supplemental References and can be found with this article at doi:10.1016/j.cmet.2011.01.018.

REFERENCES

Aird, W.C. (2007). Phenotypic heterogeneity of the endothelium. I. Structure, function, and mechanisms. Circ. Res. 100, 158–173.

Barrett, E.J., Eggleston, E.M., Inyard, A.C., Wang, H., Li, G., Chai, W., and Liu, Z. (2009). The vascular actions of insulin control its delivery to muscle and regulate the rate-limiting step in skeletal muscle insulin action. Diabetologia 52, 752–764.

Bergman, R.N. (1989). Lilly Lecture: toward physiological understanding of glucose tolerance: minimal-model approach. Diabetes 38, 1512–1527.

Brüning, J.C., Michael, M.D., Winnary, J.N., Hayashi, T., Hörsch, D., Accili, D., Goodyear, L.J., and Kahn, C.R. (1998). A muscle-specific insulin receptor knockout exhibits features of the metabolic syndrome of NIDDM without altering glucose tolerance. Mol. Cell 2, 559–569.

Chiu, J.D., Richey, J.M., Harrison, L.N., Zuniga, E., Kolk, C.M., Kirkman, E., Ellmerer, M., and Bergman, R.N. (2008). Direct administration of insulin into skeletal muscle reveals that the transport of insulin across the capillary endothelium limits the time course of insulin to activate glucose disposal. Diabetes 57, 828–835.

Clark, M.G. (2008). Impaired microvascular perfusion: a consequence of vascular dysfunction and a potential cause of insulin resistance in muscle. Am. J. Physiol. Endocrinol. Metab. 295, E732–E750.

DeFronzo, R.A., Tobin, J.D., and Andres, R. (1979). Glucose clamp technique: a method for quantifying insulin secretion and resistance. Am. J. Physiol. 237, E214–E223.

Ellmerer, M., Hamilton-Wessler, M., Kim, S.P., Huecking, K., Kirkman, E., Chiu, J., Richey, J., and Bergman, R.N. (2006). Reduced access to insulin-sensitive tissues in dogs with obesity secondary to increased fat intake. Diabetes 55, 1769–1775.

Hamilton-Wessler, M., Ader, M., Dea, M.K., Moore, D., Loftager, M., Markussen, J., and Bergman, R.N. (2002). Mode of transcapillary transport of insulin and insulin analog NN304 in dog hindlimb: evidence for passive diffusion. Diabetes 51, 574–582.

Jansson, P.A., Fowelin, J.P., von Schenck, H.P., Smith, U.P., and Lönnroth, P.N. (1993). Measurement by microdialysis of the insulin concentration in subcutaneous interstitial fluid. Importance of the endothelial barrier for insulin. Diabetes 42, 1469–1473.

Jiang, Z.Y., Lin, Y.W., Clemont, A., Feener, E.P., Hein, K.D., Igarashi, M., Yamauchi, T., White, M.F., and King, G.L. (1999). Characterization of selective resistance to insulin signaling in the vasculature of obese Zucker (fa/fa) rats. J. Clin. Invest. 104, 447–457.

Kainoh, M., Maruyama, I., Nishio, S., and Nakadate, T. (1991). Enhancement by beraprost sodium, a stable analogue of prostacyclin, in thrombomodulin expression on membrane surface of cultured vascular endothelial cells via increase in cyclic AMP level. Biochem. Pharmacol. 41, 1135–1140.

Karnieli, E., Zarnowski, M.J., Hissin, P.J., Simpson, I.A., Salans, L.B., and Cushman, S.W. (1981). Insulin-stimulated translocation of glucose transport systems in the isolated rat adipose cell. Time course, reversal, insulin concentration dependency, and relationship to glucose transport activity. J. Biol. Chem. 256, 4772–4777.

Keske, M.A., Clerk, L.H., Price, W.J., Jahn, L.A., and Barrett, E.J. (2009). Obesity blunts microvascular recruitment in human forearm muscle after a mixed meal. Diabetes Care 32, 1672–1677.

Kisanuki, Y.Y., Hammer, R.E., Miyazaki, J., Williams, S.C., Richardson, J.A., and Yanagisawa, M. (2001). Tie2-Cre transgenic mice: a new model for endothelial cell-lineage analysis in vivo. Dev. Biol. 230, 230–242.

Kubota, T., Kubota, N., Moroi, M., Terauchi, Y., Kobayashi, T., Kamata, K., Suzuki, R., Tobe, K., Namiki, A., Aizawa, S., et al. (2003). Lack of insulin receptor substrate-2 causes progressive neointima formation in response to vessel injury. Circulation 107, 3073–3080.

Kubota, N., Kubota, T., Itoh, S., Kumagai, H., Kozono, H., Takamoto, I., Mineyama, T., Ogata, H., Tokuyama, K., Ohsugi, M., et al. (2008). Dynamic functional relay between insulin receptor substrate 1 and 2 in hepatic insulin signaling during fasting and feeding. Cell Metab. 8, 49–64.

Long, Y.C., and Zierath, J.R. (2008). Influence of AMP-activated protein kinase and calcineurin on metabolic networks in skeletal muscle. Am. J. Physiol. Endocrinol. Metab. 295, E545–E552.

Miles, P.D., Levisetti, M., Reichart, D., Khoursheed, M., Moossa, A.R., and Olefsky, J.M. (1995). Kinetics of insulin action in vivo. Identification of rate limiting steps. Diabetes 44, 947–953.

Muniyappa, R., and Quon, M.J. (2007). Insulin action and insulin resistance in vascular endothelium. Curr. Opin. Clin. Nutr. Metab. Care 10, 523–530.

Niwano, K., Arai, M., Tomaru, K., Uchiyama, T., Ohyama, Y., and Kurabayashi, M. (2003). Transcriptional stimulation of the eNOS gene by the stable prostacyclin analogue beraprost is mediated through cAMP-responsive element in vascular endothelial cells: close link between PGI2 signal and NO pathways. Circ. Res. 93, 523–530.

Nolan, J.J., Ludvik, B., Baloga, J., Reichart, D., and Olefsky, J.M. (1997). Mechanisms of the kinetic defect in insulin action in obesity and NIDDM. Diabetes 46, 994–1000.

Petersen, K.F., Dufour, S., Befroy, D., Garcia, R., and Shulman, G.I. (2004). Impaired mitochondrial activity in the insulin-resistant offspring of patients with type 2 diabetes. N. Engl. J. Med. 350, 664–671.

Rattigan, S., Clark, M.G., and Barrett, E.J. (1997). Hemodynamic actions of insulin in rat skeletal muscle: evidence for capillary recruitment. Diabetes 46, 1381–1388.

Sherwin, R.S., Kramer, K.J., Tobin, J.D., Insel, P.A., Liljenquist, J.E., Berman, M., and Andres, R. (1974). A model of the kinetics of insulin in man. J. Clin. Invest. 53, 1481–1492.

Sjostrand, M., Gudbjornsdottir, S., Holmang, A., Lonn, L., Strindberg, L., and Lönnroth, P. (2002). Delayed transcapillary transport of insulin to muscle interstitial fluid in obese subjects. Diabetes 51, 2742–2748.

Vicent, D., Ilany, J., Kondo, T., Naruse, K., Fisher, S.J., Kisanuki, Y.Y., Bursell, S., Yanagisawa, M., King, G.L., and Kahn, C.R. (2003). The role of endothelial insulin signaling in the regulation of vascular tone and insulin resistance. J. Clin. Invest. 111, 1373–1380.

Vincent, M.A., Clerk, L.H., Lindner, J.R., Klibanov, A.L., Clark, M.G., Rattigan, S., and Barrett, E.J. (2004). Microvascular recruitment is an early insulin effect that regulates skeletal muscle glucose uptake in vivo. Diabetes 53, 1418–1423.

Vincent, M.A., Clerk, L.H., Rattigan, S., Clark, M.G., and Barrett, E.J. (2005). Active role for the vasculature in the delivery of insulin to skeletal muscle. Clin. Exp. Pharmacol. Physiol. 32, 302–307.

Wallis, M.G., Wheatley, C.M., Rattigan, S., Barrett, E.J., Clark, A.D.H., and Clark, M.G. (2002). Insulin-mediated hemodynamic changes are impaired in muscle of Zucker obese rats. Diabetes 51, 3492–3498.

Wang, H., Wang, A.X., Liu, Z., and Barrett, E.J. (2008). Insulin signaling stimulates insulin transport by bovine aortic endothelial cells. Diabetes 57, 540–547.

White, M.F., and Kahn, C.R. (1994). The insulin signaling system. J. Biol. Chem. 269, 1–4.

Yang, Y.J., Hope, I.D., Ader, M., and Bergman, R.N. (1989). Insulin transport across capillaries is rate limiting for insulin action in dogs. J. Clin. Invest. 84, 1620–1628.

A regulatory subunit of phosphoinositide 3-kinase increases the nuclear accumulation of X-box–binding protein-1 to modulate the unfolded protein response

Jonathon N Winnay[1], Jeremie Boucher[1,3], Marcelo A Mori[1,3], Kohjiro Ueki[2] & C Ronald Kahn[1]

Class Ia phosphoinositide 3-kinase (PI3K), an essential mediator of the metabolic actions of insulin, is composed of a catalytic (p110α or p110β) and regulatory (p85α, p85β or p55γ) subunit. Here we show that p85α interacts with X-box–binding protein-1 (XBP-1), a transcriptional mediator of the unfolded protein response (UPR), in an endoplasmic reticulum (ER) stress-dependent manner. Cell lines with knockout or knockdown of p85α show marked alterations in the UPR, including reduced ER stress–dependent accumulation of nuclear XBP-1, decreased induction of UPR target genes and increased rates of apoptosis. This is associated with a decreased activation of inositol-requiring protein-1α (IRE1α) and activating transcription factor-6α (ATF6α). Mice with deletion of p85α in liver (L-*Pik3r1*^{−/−}) show a similar attenuated UPR after tunicamycin administration, leading to an increased inflammatory response. Thus, p85α forms a previously unrecognized link between the PI3K pathway, which is central to insulin action, and the regulation of the cellular response to ER stress, a state that when unresolved leads to insulin resistance.

There is a worldwide epidemic of obesity, type 2 diabetes and metabolic syndrome, all conditions linked to insulin resistance[1,2]. Although multiple mechanisms contribute to the development of insulin resistance in these disorders, one major mechanism is the activation of cellular stress and inflammatory signaling pathways[3,4]. Understanding exactly how these stress pathways are linked to insulin signaling dynamics is crucial.

Class Ia PI3Ks are a family of lipid kinases that regulate multiple cellular processes, including cell metabolism and growth, by virtue of their ability to generate the second messenger, phosphatidylinositol-3,4,5-trisphosphate[5]. This enzyme exists as an obligate heterodimer, composed of a regulatory and catalytic subunit, both of which occur in several isoforms. The central role of this enzyme in mediating the metabolic actions of insulin is apparent from studies where expression of dominant-negative constructs or pharmacological inhibition of PI3K completely abolishes insulin stimulation of glucose transport, lipogenesis and glycogen synthesis[6,7]. Alterations in insulin stimulation of PI3K activity have been observed in mouse models of obesity, as well as in humans with type 2 diabetes[8–10].

The ER forms an interconnected, membranous network that is the major site of synthesis and folding of secreted and integral membrane proteins. Protein folding in the ER lumen is facilitated by a number of molecular chaperones, including the glucose-regulated proteins BiP and Grp94, and a variety of folding enzymes such as protein disulfide isomerase (PDI)[11,12]. Physiological states that increase protein synthesis, or stimuli that disrupt the processes by which proteins obtain their native conformation, create an imbalance between the protein-folding demand and capacity of the ER. This results in the accumulation of unfolded or improperly folded proteins in the ER lumen and a state of ER stress. The cellular response to ER stress, referred to as the UPR, results in activation of three linked signal transduction pathways emanating from three principle ER stress sensors: IRE1α, double-stranded RNA–dependent protein kinase–like kinase (PERK) and ATF6α[13,14]. The combined actions of these signaling cascades serve to reduce ER stress through attenuation of protein translation to reduce the load on the ER translational machinery and through activation of transcriptional programs that ultimately serve to increase ER protein folding and maturation.

Pathophysiological states including obesity, hyperlipidemia, nutrient deprivation, hypoxia, infection and inflammation have been shown to disrupt ER homeostasis[15–18]. For example, mice with genetic or diet-induced obesity show a considerable elevation in ER stress, with elevated phosphorylation of PERK and IRE1α and enhanced splicing of XBP-1 (ref. 19). Several markers of ER stress are also elevated in adipose tissue from obese humans[18,20]. Conversely, the increase in insulin sensitivity associated with weight loss is associated with a substantial reduction in markers of UPR activation[21]. Furthermore, mice given chemical chaperones that facilitate protein folding or transgenic mice overexpressing the ER chaperone 150-kDa oxygen-regulated protein show improvements in obesity-associated insulin resistance and glucose metabolism[22,23]. Mechanistically, activation of the UPR in the obese state contributes to the decrease in insulin sensitivity through IRE1α-dependent activation of c-Jun N-terminal kinase (JNK), which leads to phosphorylation of insulin receptor substrate-1 (IRS-1) on inhibitory serine residues[24–26].

[1]Section on Integrative Physiology and Metabolism, Research Division, Joslin Diabetes Center, Harvard Medical School, Boston, Massachusetts, USA. [2]Department of Metabolic Diseases, Graduate School of Medicine, The University of Tokyo, Tokyo, Japan. [3]These authors contributed equally to this work. Correspondence should be addressed to C.R.K. (c.ronald.kahn@joslin.harvard.edu).

Figure 1 Identification and characterization of XBP-1 as a p85α interacting protein. (**a**) Top, schematic diagram of the plasmids used in the bacterial two-hybrid screen. SH2 and SH3, Src-homology-2 and Src-homolgy-3, respectively; BH, Bcl-2 homology; λCl, bacteriophage λ repressor protein. Bottom, schematic of the XBP-1 cDNA and the alternative splice variants that generate open reading frames (ORF 1 and ORF 2) that encode XBP-1u and XBP-1s, respectively. b-ZIP, basic leucine zipper. (**b**) Coimmunoprecipitation experiments performed on HEK293 cells transfected with HA-p85α alone or in combination with Flag–XBP-1u or Flag–XBP-1s. HA immunoprecipitates (IP) were immunoblotted with Flag-specific antibodies. Immunoblotting (IB) with actin–specific antibody confirmed equal protein was used for each condition. (**c**) Flag-specific immunoblotting of HEK 293T cells

transiently transfected with expression plasmids encoding the indicated proteins. Forty-eight hours after transfection, cytosolic and nuclear lysates were prepared. (**d**) The nucleocytoplasmic shuttling of Flag–XBP-1s, as assessed in HEK293T cells transfected with or without Flag–XBP-1s and increasing concentrations of HA-p85α expression plasmid. Nuclear and cytoplasmic fractions were immunoblotted with Flag or HA antibodies.
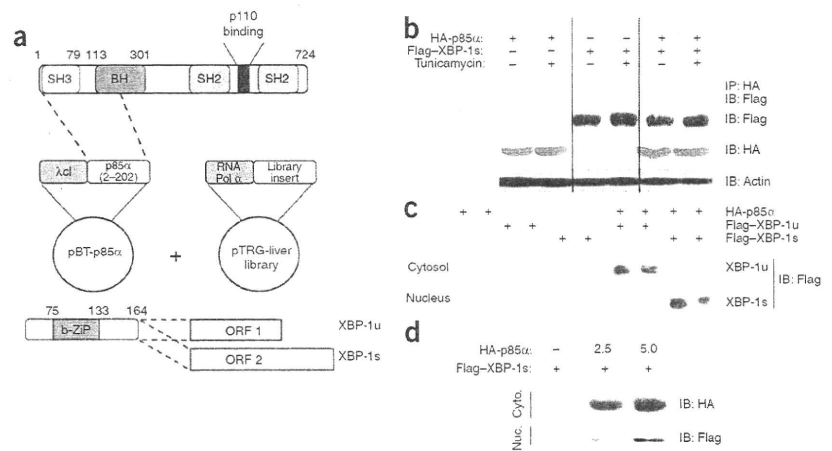
Additional evidence establishing a mechanistic link between IRE1α and UPR-associated insulin resistance comes from studies of mice haploinsufficient for XBP-1. Normally, in response to ER stress, IRE1α executes site-specific cleavage of XBP-1 messenger RNA to produce a transcript (XBP-1s) that encodes a potent transcriptional activator of UPR target genes[27,28]. When subjected to a high-fat diet, XBP-1–heterozygous mice gain more weight and become more insulin resistant than control mice[19]. These mice also show an increase in ER stress in adipose tissue, with enhanced PERK and IRE1α phosphorylation and activation of JNK. Likewise, XBP-1–deficient fibroblasts show enhanced PERK phosphorylation, hyperactivation of JNK and increased serine phosphorylation of IRS-1 (ref. 19). Collectively, these data demonstrate how the ER stress response and alterations in XBP-1 can modulate insulin sensitivity.

Here we show another link between insulin signaling and the UPR. We show that the p85α regulatory subunit of PI3K interacts with XBP-1 in an ER stress–dependent manner and that this interaction is essential in the ER stress response. As a result, cells deficient in p85α or livers with selective inactivation of the gene encoding p85α show a marked reduction in ER stress and accumulation of nuclear XBP-1s protein and its downstream target proteins. This link between the regulatory subunit of PI3K and the cellular response to ER stress provides a new therapeutic target for the treatment of diseases in which the UPR is activated, such as obesity and type 2 diabetes.

RESULTS

p85α associates with an XBP-1–containing protein complex

In previous studies, we have shown that deletion of the p85α subunit of PI3K results in decreased activation of JNK and increased insulin sensitivity and that this depends on the N-terminal half of p85α and is independent of its role in PI3K activation[29–31]. To identify proteins that interact with the N-terminal region of p85α, we performed an interaction screen with a bacterial two-hybrid system and a human liver complementary DNA library (**Fig. 1a**). Sequencing of isolated cDNA clones revealed that one p85α interacting partner was the transcription factor XBP-1. The XBP-1–interacting cDNA encoded the NH$_2$-terminal portion of the XBP-1 protein, a region shared between the unspliced (XBP-1u) and spliced (XBP-1s) isoforms (**Fig. 1a**).

To confirm that the association between p85α and XBP-1 observed in the bacterial two-hybrid screen could also occur in mammalian cells, we performed coimmunoprecipitation experiments with extracts of cells transfected with HA-p85α and Flag–XBP-1s expression plasmids alone or in combination (**Fig. 1b**). Although we did not find XBP-1 in HA immunoprecipitates from cells transfected with HA-p85α or Flag–XBP-1s alone, we found abundant Flag–XBP-1s in HA-p85α immunoprecipitates when both proteins were expressed (**Fig. 1b**). Notably, there was a marked reduction in the association between XBP-1s and p85α after treatment with tunicamycin, suggesting that this interaction is regulated by ER stress (**Fig. 1b**). We obtained similar results when we infected rat hepatoma cells with adenoviruses expressing either GFP or p85α with an N-terminal tandem affinity purification (TAP) tag containing the streptavidin and calmodulin binding domains (**Supplementary Fig. 1**)[32,33]. These data demonstrate that p85α and XBP-1 physically associate and that this interaction is modulated by the cellular response to ER stress.

p85α promotes stabilization and nuclear accumulation of XBP-1

Degradation of XBP-1 involves both ubiquitin-dependent and ubiquitin-independent mechanisms, resulting in short half-lives of both the XBP-1u and the XBP-1s proteins[34]. To determine whether p85α alters the stability of XBP-1, we transiently transfected HEK293 cells with plasmids encoding XBP-1 or p85α either alone or in combination. Concurrent expression of XBP-1 with p85α led to a substantial increase in the amount of XBP-1u and XBP-1s in the cytoplasm and nucleus, respectively (**Fig. 1c**).

In contrast to XBP-1u, XBP-1s is primarily localized to the nucleus. Expression of an N-terminal deletion of XBP-1s leads to its redistribution to both the cytoplasm and the nucleus, suggesting that this region of XBP-1s governs its nuclear localization[34,35]. Having established that p85α and XBP-1 interact and that the interaction occurs between the N-terminal portion of p85α and the shared N-terminal fragment of XBP-1 capable of directing nuclear localization, we examined whether p85α is able to alter the cellular distribution of XBP-1. To this end, we transiently transfected cells with Flag–XBP-1s in the absence or presence of increasing amounts of HA-p85α and performed immunoblotting on cytoplasmic and nuclear fractions with Flag-specific antibodies. Notably, the dose-dependent increase
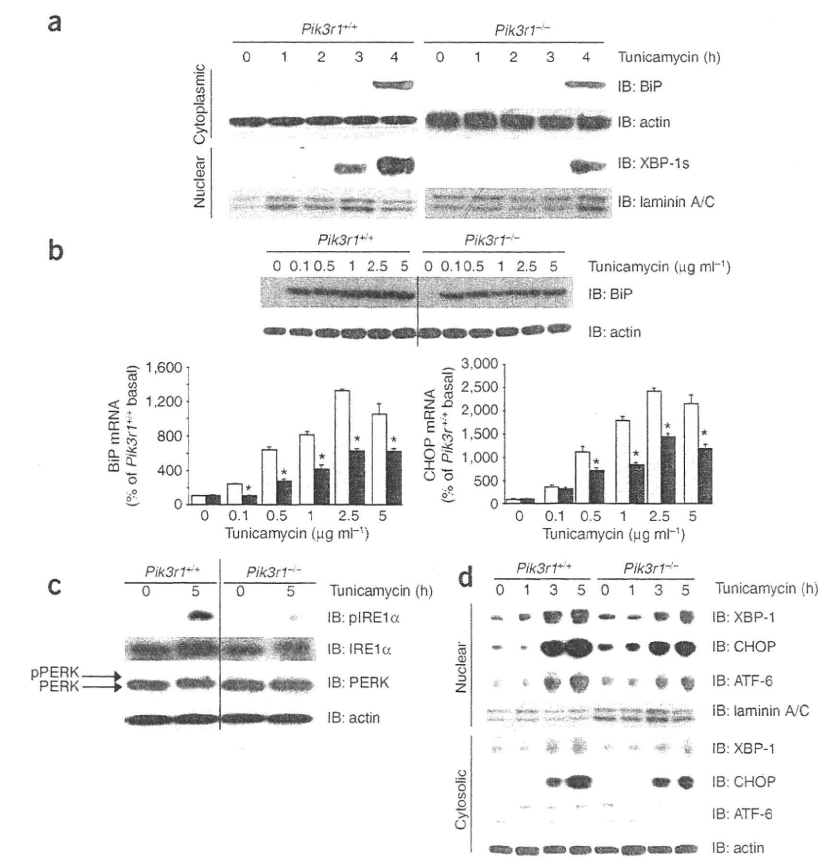
Figure 2 Evaluation of ER stress and UPR signaling dynamics in p85α-deficient fibroblasts. (**a**) Immunoblots of cytoplasmic and nuclear protein fractions to assess the induction of BiP or XBP-1s protein, respectively, over a time-course of tunicamycin (2 μg ml⁻¹) treatment. (**b**) Top, BiP-specific immunoblots of whole-cell lysates of control and *Pik3r1⁻/⁻* fibroblasts treated with the indicated concentrations of tunicamycin for 5 h. Actin-specific immunoblotting were performed to ensure equal loading. Bottom, quantitative RT-PCR analysis of cDNA derived from control and *Pik3r1⁻/⁻* fibroblasts treated with the indicated concentrations of tunicamycin for 5 h. (**c**) Immunoblotting of whole-cell lysates with IRE1α-, pIRE1α- and PERK-specific antibodies. Control and *Pik3r1⁻/⁻* fibroblasts were treated with vehicle or tunicamycin (2 μg ml⁻¹) for 5 h. Actin-specific immunoblotting was performed to confirm equal protein loading. (**d**) Immunoblot analysis on nuclear lysates with XPB-1-, ATF6- and CHOP-specific antibodies. Control and *Pik3r1⁻/⁻* fibroblasts were treated with tunicamycin (2 μg ml⁻¹) over the indicated time course. Laminin A/C–specific immunoblotting was performed to confirm equal loading. Data are presented as the means ± s.e.m., and asterisks indicate statistical significance determined by Student's t test ($^*P < 0.05$, n = 3 experiments).

in HA-p85α resulted in a parallel increase in the nuclear translocation of XBP-1s (**Fig. 1d**). Thus, increasing the abundance of p85α leads to the stabilization of XBP-1 and enhances the nucleocytoplasmic shuttling of XBP-1.

Fibroblasts lacking p85α show an altered response to ER stress

Given the central role of XBP-1 as a mediator of the UPR, we sought to determine whether the interaction between p85α and XBP-1 is involved in control of the cellular response to ER stress. We treated immortalized control (*Pik3r1⁺/⁺*) and p85α-deficient (*Pik3r1⁻/⁻*) brown preadipocyte cell lines[29] with vehicle or tunicamycin and assessed BiP and XBP-1s protein expression in cytoplasmic or nuclear compartments (**Fig. 2a**). As expected, treatment of control preadipocytes with tunicamycin for 4 h resulted in the appearance of BiP, and immunoblots performed on nuclear lysates revealed a time-dependent accumulation of XBP-1s (**Fig. 2a**). By contrast, when we treated *Pik3r1⁻/⁻* cells with tunicamycin, BiP induction was reduced by 50%, and there was markedly less nuclear accumulation of XBP-1s, with no detectable nuclear XBP-1s at 3 h and a 40% reduction in nuclear XBP-1s after 4 h when compared to *Pik3r⁺/⁺* cells treated in parallel (**Fig. 2a**). Thus, the absence of p85α alters the cellular response to ER stress with a decrease in nuclear accumulation of XBP-1s and reduced expression of BiP.

To exclude the possibility that the defect observed in *Pik3r1⁻/⁻* cells is the result of reduced sensitivity to UPR activation, we performed a dose-response analysis with tunicamycin. As expected, *Pik3r1⁺/⁺* cells showed a dose-dependent increase in BiP expression after treatment with 0.1–5 μg ml⁻¹ tunicamycin (**Fig. 2b**). In *Pik3r1⁻/⁻* cells treated

with tunicamycin, BiP protein expression showed a dose-dependent increase; however, BiP amounts were 50–60% lower at all tunicamycin concentrations (**Fig. 2b**). Likewise, there was a dose-dependent 10- to 20-fold increase in BiP and the ER stress–induced transcription factor C/EBP-homologous protein (CHOP) mRNA levels after tunicamycin treatment in control cells, whereas p85α-deficient cells showed a 50–60% reduction in BiP and CHOP mRNA levels at all concentrations (**Fig. 2b**). We observed a similar reduction in the UPR targets BiP and CHOP at the mRNA and protein levels when we used thapsigargin to activate the UPR (**Supplementary Figs. 2** and **3** and data not shown). These effects were independent of PI3K enzyme activity, as pharmacological inhibition of PI3K with LY294002 had no effect on the induction of BiP expression after tunicamycin or thapsigargin treatment (**Supplementary Fig. 4**). In addition, attempts to coimmunoprecipitate p110α and XBP-1 failed to identify an interaction, thereby providing an additional indication that the role of p85α as it relates to XBP-1 function is independent of p110α action.

UPR pathways are altered in p85α-deficient fibroblasts

Given the above results, it was clear that p85α deficiency severely impairs the cellular response to ER stress, with reduced expression of BiP and nuclear accumulation of XBP-1s in response to UPR activation. p85α deficiency was also associated with alterations in IRE1α- and ATF6α-dependent signaling pathways. Thus, whereas control cells responded to tunicamycin treatment with a considerable upregulation of IRE1α protein and an enhancement of IRE1α phosphorylation, *Pik3r1⁻/⁻* cells showed an ~20–40% reduction of IRE1α expression in the basal state and after tunicamycin treatment and an associated reduction in IRE1α phosphorylation (**Fig. 2c**). Notably, although we readily observed alteration in IRE1α activation, there were no

Figure 3 Evaluation of XBP-1 target-gene transcription, UPR-dependent gene expression and apoptosis. (**a**) Quantitative PCR of mRNA expression of UPR target genes in *Pik3r1*^{+/+} or *Pik3r1*^{−/−} cells treated with vehicle or tunicamycin for 5 h. (**b**) FACS analysis to determine the percentage of apoptotic cells (PI-negative, annexin-PE–positive cells) among cells grown to confluence and maintained in 10% FBS supplemented with or without tunicamycin (2 µg ml^{−1}) or thapsigargin (100 nM) for 24 h. Data are means ± s.e.m. from three independent experiments. (**c**) Quantitative PCR analysis of control and shp85α cell lines with *Pik3r1*-specific primers. (**d**) Immunoblot analysis of whole-cell lysates prepared from shGFP and shp85α cell lines treated with vehicle or tunicamycin (2 µg ml^{−1}) for 5 h. (**e**) Quantitative PCR analysis of BiP, Erdj4 and Grp94 mRNA expression in shGFP and shp85α cell lines before or after treatment with tunicamycin (2 µg ml^{−1}) for 5 h. Data are presented as the means ± s.e.m., and asterisks indicate statistical significance determined by Student's *t* test (*$P < 0.05$; **$P < 0.001$; ***$P < 0.005$; n.s., not significant) ($n = 3$ experiments). Significance is relative to basal conditions for each cell line unless otherwise indicated with bars.
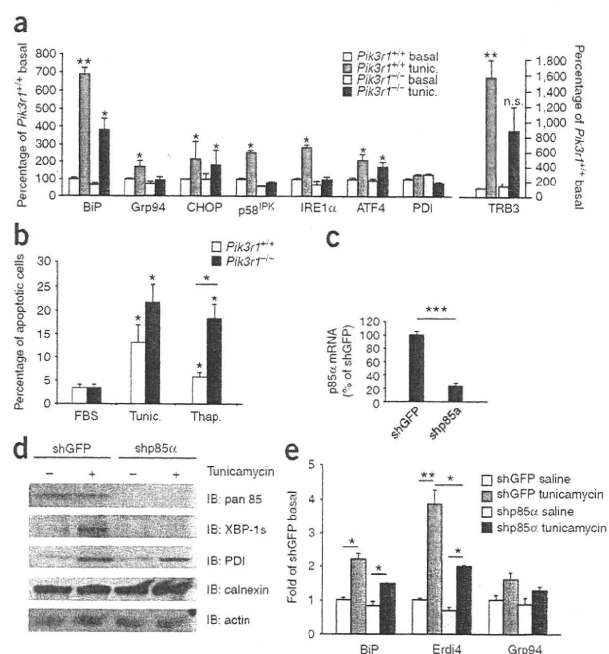
differences in PERK abundance or activation between control and *Pik3r1*^{−/−} cells, as assessed by alterations in PERK mobility or phosphorylation (**Fig. 2c** and data not shown). Activation of ATF6α, as assessed by immunoblot analysis of the processed form of ATF6α in nuclear lysates, was also markedly attenuated in *Pik3r1*^{−/−} cells at the 3-h and 5-h time points and paralleled the blunted response in accumulation of nuclear XBP-1s and induction of CHOP (**Fig. 2d**). Thus, p85α deficiency attenuates the cellular response to ER stress through multiple mechanisms involving alterations in the induction of XBP-1s and activation of IRE1α- and ATF6-dependent pathways.

XBP-1 splicing and UPR gene expression in *Pik3r1*^{−/−} cells

To examine whether alterations in the IRE1α pathway lead to a reduction in XBP-1 splicing capacity in *Pik3r1*^{−/−} fibroblasts, we performed an XBP-1 splicing assay. As expected, untreated control fibroblasts produced primarily the XBP-1u transcript, with only a small amount of XBP-1 migrating at the expected size of the spliced transcript (**Supplementary Fig. 5a**). Treatment of these cells with tunicamycin resulted in a marked decrease in XBP-1u and a concomitant increase in XBP-1s transcript levels (**Supplementary Fig. 5a**). In contrast, *Pik3r1*^{−/−} cells showed a reduction in XBP-1u transcript levels in the basal state and a relatively modest increase in spliced XBP-1 transcript levels after treatment with tunicamycin (**Supplementary Fig. 5a**). Quantitative PCR analysis showed a 2.5-fold increase in total XBP-1 transcript levels after tunicamycin treatment in control cells (**Supplementary Fig. 5b**, $P < 0.05$). In p85α-deficient cells, total XBP-1 transcript levels were reduced by 50% in the basal state, and there was a significantly attenuated, tunicamycin-dependent increase when compared to controls. (**Supplementary Fig. 5b**, $P < 0.001$). Likewise, in control cells, tunicamycin produced an ~30-fold increase in XBP-1s mRNA levels (100% ± 2.45% versus 3,067% ± 778%, vehicle versus tunicamycin, percentage of *Pik3r1*^{+/+} vehicle), and this response was markedly blunted in p85α-deficient cells (91% ± 29% versus 1,181% ± 193%, vehicle versus tunicamycin, percentage of *Pik3r1*^{+/+} vehicle) (**Supplementary Fig. 5b**). Thus, p85α deficiency decreases IRE1α-dependent XBP-1 splicing in response to ER stress.

We next sought to establish the extent to which the defects in IRE1α protein and phosphorylation and decreased transcription and splicing of XBP-1 mRNA in *Pik3r1*^{−/−} cells alters the induction of UPR target genes. Analysis of control fibroblasts treated with tunicamycin for 5 h revealed 50–60% increases in the expression of multiple mRNAs for UPR targets, including BiP, Grp94, CHOP, protein kinase inhibitor of

58 kDa (p58[IPK]), IRE1α, ATF4 and Tribbles homolog-3 (TRB3) (**Fig. 3a**). In contrast, the transcriptional profile in *Pik3r1*^{−/−} cells could be classified into two distinct categories. The first included mRNAs such as BiP, CHOP and ATF4 that were upregulated by tunicamycin but to a much lower level than that achieved in control cells (**Fig. 3a**). The second included mRNAs whose expression was significantly elevated in control cells after induction of ER stress, including Grp94 ($P < 0.05$), p58[IPK] ($P < 0.05$), IRE1α ($P < 0.05$) and TRB3 ($P < 0.01$), but showed a nonsignificant increase in *Pik3r1*^{−/−} cells after treatment with tunicamycin (**Fig. 3a**).

Lastly, to evaluate the outcome of blunted UPR activation in p85α-deficient cells, we measured apoptosis in control and *Pik3r1*^{−/−} preadipocytes after treatment with tunicamycin and thapsigargin (**Fig. 3b** and **Supplementary Fig. 6**). As expected, treatment of *Pik3r1*^{+/+} and *Pik3r1*^{−/−} cells for 24 h with tunicamycin or thapsigargin increased the rates of apoptosis when compared to cells grown in normal medium (**Fig. 3b** and **Supplementary Fig. 6**). Of note, a higher proportion of p85α-deficient cells became apoptotic after treatment with tunicamycin (13.1% ± 3.7% versus 21.6% ± 3.5%, *Pik3r1*^{+/+} versus *Pik3r1*^{−/−}) and thapsigargin (5.8% ± 0.9% versus 18.2% ± 3.0%). Thus, by all criteria tested, p85α-deficient cells show a failure to normally activate the UPR and resolve ER stress. This dysfunction leads to deleterious outcomes, including a propensity to enter apoptotic programs.

Lowering p85α expression in Huh7 cells alters the UPR

We observed similar effects of p85α deficiency in human Huh7 hepatoma cells after lentivirus-mediated short hairpin RNA knockdown of p85α mRNA. With this approach, we achieved a 78% decrease in p85α mRNA levels when compared to control cells expressing shRNA specific for GFP (shGFP) (**Fig. 3c**), and we confirmed this by immunoblot analysis with p85α-specific antibodies (**Fig. 3d**). Control cells exposed to tunicamycin also showed a marked increase in XBP-1s protein abundance, whereas we did not detect any XBP-1 in cells after p85α knockdown (**Fig. 3d**). In addition, there was an attenuated increase in PDI in p85α-deficient cells (**Fig. 3d**). Similarly, treatment
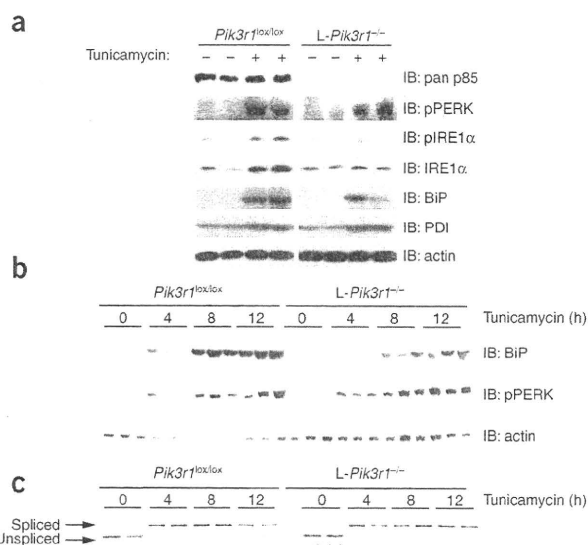
a

b

c

Figure 4 Evaluation of the UPR in livers from control and L-$Pik3r1^{-/-}$ mice. At 8 weeks of age, male $Pik3r1^{lox/lox}$ or L-$Pik3r1^{-/-}$ mice were given vehicle or tunicamycin (2.5 µg per g body weight) by intraperitoneal injection. (**a,b**) After 72 h (n = 4 per group) (**a**) or a short time-course (**b**) of tunicamycin administration, livers were collected and tissue lysates prepared. Immunoblotting was performed with antibodies to the indicated proteins. Actin immunoblotting was performed to confirm equal protein loading. (**c**) XBP-1 splicing was evaluated by PCR on cDNA derived from livers of control and L-$Pik3r1^{-/-}$ mice treated with vehicle or tunicamycin for 4, 8 or 12 h.

of shGFP cells with tunicamycin led to a robust transition from the XBP-1u to XBP-1s transcript, whereas splicing of the XBP-1 transcript after tunicamycin treatment was diminished in cells expressing shRNA to p85α (shp85α), as reflected by lower levels of XBP-1s transcript and an associated increase in XBP-1u mRNA when compared with controls (**Supplementary Fig. 5c**). As a result, the tunicamycin-dependent induction of the UPR target proteins endoplasmic reticulum DnaJ homolog-4 (ERdj4) and BiP was attenuated in shp85α cells when compared to controls (**Fig. 3e**). Thus, p85α deficiency alters the cellular response to ER stress independently of cell type or stimulus, indicating a major role of the interaction between p85α and XBP-1 in ER stress induction and the UPR.

A blunted UPR is observed in livers of L-$Pik3r1^{-/-}$ mice

To determine whether the effects observed *in vitro* would be recapitulated *in vivo*, we used mice in which the $Pik3r1$ gene is selectively inactivated in liver by the Cre-$loxP$ system (L-$Pik3r1^{-/-}$ mice). At 2 months of age, we gave male mice vehicle or tunicamycin (2.5 µg per g body weight) and, after 72 h, collected livers for analysis.

Immunoblots confirmed the absence of p85α in lysates from vehicle- and tunicamycin-treated L-$Pik3r1^{-/-}$ mice (**Fig. 4a**). As anticipated, PERK and IRE1α phosphorylation was low in vehicle-treated L-$Pik3r1^{lox/lox}$ mice, but it increased substantially after tunicamycin administration (**Fig. 4a**). In contrast, livers from L-$Pik3r1^{-/-}$ mice had undetectable basal IRE1α phosphorylation and a markedly blunted, tunicamycin-dependent increase in IRE1α phosphorylation, with no considerable alteration in activation of the PERK pathway (**Fig. 4a**). There was also a marked, tunicamycin-dependent increase in total IRE1α and BiP protein abundance in control mice, and these responses were severely blunted in L-$Pik3r1^{-/-}$ mice (**Fig. 4a**). We observed a similar blunting of the UPR and reduced activation of the ATF6α pathway 18 h after administration of tunicamycin (**Supplementary Fig. 7**). Likewise, as early as 4 h after tunicamycin administration, the increase in BiP protein was significantly blunted in p85α-deficient livers when compared to controls (347.5% versus 131.8%, L-$Pik3r1^{+/+}$ versus L-$Pik3r1^{-/-}$, $P < 0.05$), despite normal activation of the PERK pathway (**Fig. 4b**). Thus, activation of the IRE1α and ATF6α pathways and the ER stress response pathways are impaired in the livers of p85α-deficient mice. Unlike the defect observed in $Pik3r1^{-/-}$ cells, this impairment occurred independently of alterations in XBP-1 splicing (**Fig. 4c**).

The attenuated response to ER stress in livers from L-$Pik3r1^{-/-}$ mice was accompanied by altered expression of UPR-dependent target genes. In liver of control mice, BiP mRNA expression increased fivefold (100% ± 8.2% versus 579% ± 131%) in response to tunicamycin treatment, whereas in L-$Pik3r1^{-/-}$ mice the increase in BiP was reduced by ~50% and failed to reach statistical significance (**Fig. 5a**). Likewise, in control mice, tunicamycin elicited a threefold increase in p58^{IPK} mRNA (100% ± 10.1% versus 288% ± 39.6%,
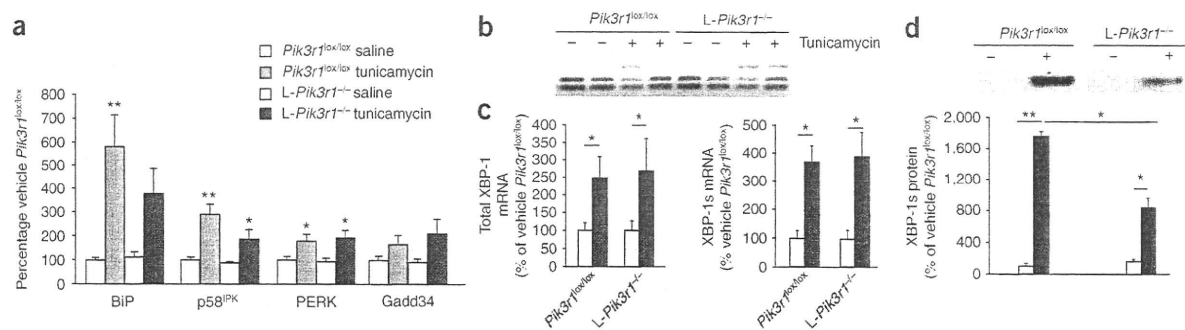

Figure 5 Analysis of gene expression, XBP-1 splicing and XBP-1 stability in livers from $Pik3r1^{lox/lox}$ and L-$Pik3r1^{-/-}$ mice after 72 h of vehicle or tunicamycin treatment (n = 5 per group). (**a**) UPR-dependent target gene expression, as determined by quantitative PCR on cDNA derived from $Pik3r1^{lox/lox}$ and L-$Pik3r1^{-/-}$ livers with gene-specific primers. (**b**) A PCR-based assay to evaluate XBP-1 splicing. (**c**) XBP-1 splicing in the livers from saline- and tunicamycin-treated (2.5 µg per g body weight) mice, as assessed by quantitative PCR as previously described[58]. (**d**) Top, immunoblot analysis of nuclear lysates from $Pik3r1^{lox/lox}$ and L-$Pik3r1^{-/-}$ mice after 18 h of tunicamycin (2.5 µg per g body weight) treatment with XBP-1–specific antibodies. Bottom, quantification of nuclear XBP-1s protein by densitometry. Data are presented as the means ± s.e.m., and asterisks indicate statistical significance determined by Student's t test ($^*P < 0.05$; $^{**}P < 0.001$, n = 5 or 6 per group).
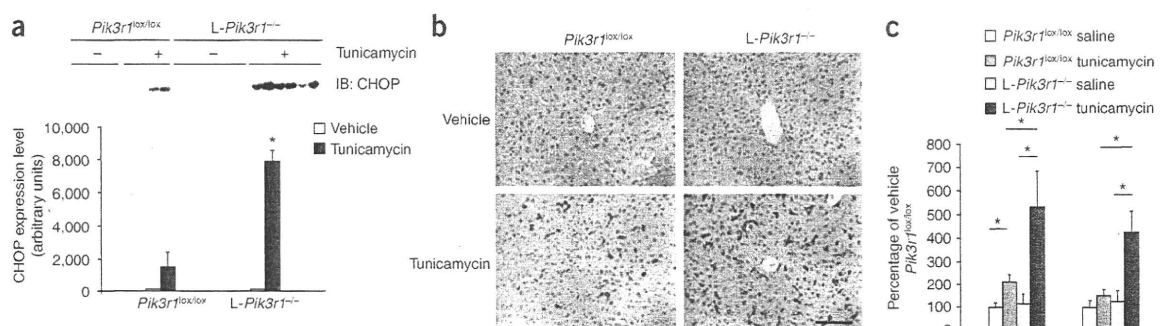
- 563 -

Figure 6 Analysis of liver from control and L-Pik3r1^{-/-} mice after tunicamycin treatment. (**a**) CHOP protein expression, as assessed 18 h after tunicamycin treatment by SDS-PAGE on liver lysates followed by immunoblotting with CHOP-specific antibodies. (**b**) Immunohistochemical analysis of livers from control and L-Pik3r1^{-/-} mice with F4/80-specific antibodies. Representative images are shown. $n = 5$ per group. Scale bar, 50 μm. (**c**) The expression of CD68 and TNF-α, as determined by quantitative PCR on cDNA derived from livers from control and L-Pik3r1^{-/-} mice 36 h after administration of vehicle or tunicamycin (2 μg per g body weight). Data are presented as the means ± s.e.m., and asterisks indicate statistical significance determined by Student's t test ($^*P < 0.05$).

$P < 0.001$), and this response was blunted in the livers of L-Pik3r1^{-/-} mice ($88.2\% \pm 5.2\%$ versus $187\% \pm 39\%$, $P < 0.05$).

We did observe some differences between the *in vivo* and *in vitro* studies. Thus, *in vivo* PERK and growth arrest– and DNA damage–inducible-34 (Gadd34) mRNA levels were elevated to a similar extent in livers from L-Pik3r1[lox/lox] and L-Pik3r1^{-/-} mice after tunicamycin treatment. In addition, tunicamycin administration *in vivo* caused a comparable increase in XBP-1 splicing in L-Pik3r1[lox/lox] and L-Pik3r1^{-/-} mice (**Fig. 5b,c**). In contrast, the robust 17-fold increase (100 ± 39.4 versus $1,749 \pm 74.4$) in the nuclear XBP-1s protein in controls after tunicamycin treatment was blunted by >50% ($160\% \pm 25.9\%$ versus $830\% \pm 117\%$) in livers of L-Pik3r1^{-/-} mice (**Fig. 5d**). Thus, deletion of p85α does not affect all UPR-dependent pathways equally, and the extent of pathway involvement can be affected by other aspects of cellular context.

L-Pik3r1^{-/-} livers fail to adequately resolve ER stress
To evaluate the outcomes associated with impairment in the UPR of L-Pik3r1^{-/-} mice, we assessed apoptosis in the liver after tunicamycin administration. To our surprise, despite the increase in CHOP induction in the livers of L-Pik3r1^{-/-} mice relative to L-Pik3r1[lox/lox] mice after 18 h (**Fig. 6a**) (11.7 ± 7.3 versus 54 ± 17.7) or 36 h (data not shown) (1.5 ± 0.4 versus 16.8 ± 6.8) of treatment, we could not detect any increases in apoptosis by TUNEL or by immunoblot analysis of cleaved caspase-3 (data not shown). Histological analysis, however, revealed marked changes in livers from tunicamycin-treated L-Pik3r1^{-/-} mice, including edema and dilation of the sinusoids and bile ducts, when compared to vehicle-treated controls (**Supplementary Fig. 8**). In contrast, the livers of Pik3r1[lox/lox] mice treated with vehicle or tunicamycin appeared normal (**Supplementary Fig. 8**).

One pathological outcome of unresolved stress in the liver is an inflammatory response. Immunohistochemistry of liver sections with antibodies to the macrophage marker F4/80 revealed only sporadic staining in vehicle-treated control and L-Pik3r1^{-/-} livers (**Fig. 6b**). After tunicamycin treatment, there were more F4/80^{+} cells in the livers of Pik3r1[lox/lox] mice, whereas there was a marked increase in the number of F4/80^{+} cells in L-Pik3r1^{-/-} livers when compared to controls (**Fig. 6b**). Analysis of mRNA expression revealed a parallel change in the macrophage marker CD68 and the inflammatory cytokine tumor necrosis factor-α (TNF-α) (**Fig. 6c**). Consistent with increased macrophage recruitment, livers from L-Pik3r1^{-/-} mice also showed greater activation of the nuclear factor-κB pathway compared

to controls, as revealed by a reduction in inhibitor of κB expression after tunicamycin administration (-36.6% versus -18.6%, L-Pik3r1[lox/lox] versus L-Pik3r1^{-/-} relative to saline control) (**Supplementary Fig. 8**). These data suggest that p85α deficiency alters the fundamental ability of the liver to resolve ER stress, leading to pathological states of inflammation.

DISCUSSION
The ER stress response has been strongly implicated in the pathophysiology of diabetes, affecting both insulin sensitivity in liver and fat, and the survival of pancreatic beta cells[36–39]. Adipose tissues from obese, insulin-resistant mice and humans show a persistent low level of inflammation and activation of ER stress pathways, including induction of the UPR[4,19,40]. Identifying points of regulatory convergence that can serve as therapeutic targets to improve insulin sensitivity and relieve ER stress associated with obesity is therefore of great necessity.

Previous studies have demonstrated that PI3K is central to the actions of insulin, as well as other hormones and growth factors[6,7,41,42]. Although induction of ER stress has been shown to reduce insulin-stimulated AKT activation and decrease insulin receptor substrate tyrosine phosphorylation[19], to date there has been no evidence establishing a direct link between the PI3K pathway and ER stress. In this study, we show a new and unexpected role for the p85α regulatory subunit of PI3K as a crucial modulator of the cellular response to ER stress. This occurs via a mechanism involving p85α-dependent regulation of XBP-1s protein expression, XBP-1s nuclear translocation and ATF6α activation. Because the level of p85α can change in some insulin-resistant states, including obesity, pregnancy[43] and states of growth hormone excess[44,45], as well as in some cancers[46,47], a link between p85α and the cellular response to ER stress has major implications for understanding of a broad range of UPR-associated diseases, including diabetes, cancer and a variety of other disorders.

Our data demonstrate that p85α and XBP-1 physically associate and that this interaction modulates the cellular response to ER stress. Our identification of XBP-1 as a p85α-interacting partner with the bacterial two-hybrid system indicates that the association is direct. Our coprecipitation experiments reveal that p85α and XBP-1s interact in a protein complex that dissociates after treatment with tunicamycin, indicating that this interaction is dynamically regulated by ER stress. Although the precise mechanisms regulating

443

this interaction remain to be elucidated, the physical interaction clearly involves the N-terminal portion of p85α and a domain shared by both XBP-1 isoforms. The N-terminal region of p85α has also been shown to bind several other protein partners, including c-Cbl (a substrate for the insulin receptor kinase), the small GTPase Rac1 and cell division control protein-42, indicating a number of key roles for the p85α regulatory subunit of PI3K in addition to its role as a partner in the p85-p110 heterodimer[48,49].

The interaction between p85 and XBP-1s alters the UPR through several mechanisms. Enforced expression of p85α leads to an increase in XBP-1 protein stability and enhanced nuclear accumulation of XBP-1s. Conversely, deficiency or reduction in p85α expression in cultured cells results in a considerably attenuated UPR. This includes a reduction in IRE1α and ATF6 pathway activation and a concomitant reduction in the expression of UPR targets at the mRNA and protein levels. This is accompanied by a marked reduction in nuclear accumulation of XBP-1s after treatment with tunicamycin. Collectively, these changes are associated with a relative failure of p85α-deficient cells to resolve ER stress, as indicated by a substantial increase in apoptosis after induction of ER stress.

We also found alterations in the UPR in mice with a liver-specific deletion of p85α, including a reduced induction of the UPR targets BiP, Grp94 and CHOP at both the mRNA and protein levels. L-$Pik3r1^{-/-}$ mice also show a reduction in IRE1α expression and activation and a marked reduction in accumulation of XBP-1s in the nucleus after induction of ER stress. In contrast to isolated cells, we did not observe any alteration in XBP-1 splicing in the livers of L-$Pik3r1^{-/-}$ mice after acute stimulation with tunicamycin. These data are in accordance with the study by Park et al.[50] in this issue, which indicates that enforced expression of either p85α or p85β leads to an increase in XBP-1s nuclear localization, whereas knockdown of both regulatory subunits leads to a reduction in the nuclear accumulation of XBP-1s, providing further evidence for a critical role of PI3K regulatory subunits in modulating the UPR. Thus, lowering expression of p85α can modify the UPR by several mechanisms, including a reduction in XBP-1 protein abundance due to altered protein stabilization, decreased nuclear translocation, a reduction in total and activated IRE1α and a decrease in ATF6α pathway activation. Recent analysis of ATF6α-deficient fibroblasts has revealed that ATF6α action is crucial for the UPR-dependent transcription of ER chaperones and that heterodimerization of ATF6α and XBP-1 mediate transcriptional induction of endoplasmic reticulum–associated protein degradation genes[51]. Thus, further studies exploring the interplay between p85α, ATF6α activation and XBP-1 will be crucial in identifying other points of regulatory convergence.

The magnitude of the decrease in XBP-1s in response to decreases in p85α is comparable to or greater than that observed in XBP-1 haploinsufficient mice, suggesting that the UPR perturbations resulting from decreased p85α expression may have a similar underlying mechanism; that is, a decline in XBP-1 expression. XBP-1 heterozygous knockout mice have shown signs of elevated ER stress and have reduced insulin signaling and an associated decrease in whole-body insulin sensitivity when placed on a high-fat diet[19]. However, XBP-1–haploinsufficient mice fed a normal diet show normal plasma insulin, C-peptide and glucose concentrations, suggesting that an additional lesion is required to unmask a metabolic phenotype[19]. By comparison, mice with heterozygous deletion of p85α, homozygous inactivation of p85β or targeted deletion of p85α in liver show enhanced, rather than diminished, insulin sensitivity[52–54]. These data suggest that, given the blunted nuclear accumulation of XBP-1s in the liver cells of

L-$Pik3r1^{-/-}$ mice upon experimentally induced ER stress, it is likely that XBP-1 and p85α haploinsufficiency regulate insulin sensitivity through multifactorial and at least partially distinct pathways or that obesity may be required to unmask XBP-1–dependent insulin resistance.

Over the past decade, it has become clear that inflammation is a common feature of obesity and type 2 diabetes[40,55,56]. In obese mice, there is a ~50% reduction in p85α expression in liver[57]. These mice also show signs of heightened ER stress, including enhanced PERK phosphorylation, increased BiP expression and JNK1 activation[19]. Although there are many factors contributing to the insulin resistance in obesity, these data suggest a model where decreases in p85α lead to a reduced cellular response to ER stress via a reduction in XBP-1 stability, nuclear translocation or both and a concomitant decrease in ATF6α pathway activation.

One might predict that the failure of L-$Pik3r1^{-/-}$ mice to adequately resolve ER stress could, over long periods of time, lead to an enhanced inflammatory response. In this regard, we have found that, on prolonged follow-up, L-$Pik3r1^{-/-}$ mice develop progressive inflammatory changes in the liver that culminates in the development of hepatoma (C.Taniguchi, J.N.W., T.Kondo, R.T.Bronson, A.R.Guimaraes et al., unpublished data). UPR dysregulation may underlie the ability of tumors to escape hypoxia-induced apoptosis and may also have a key role in other diseases, including Huntington's disease, Parkinson's disease, amyotrophic lateral sclerosis and Alzheimer's disease. Further studies will be needed to determine whether the UPR in these disorders is regulated in a p85-dependent fashion and whether altering p85 expression may be a therapeutic approach to reducing the effects of the UPR in disease pathogenesis.

METHODS

Methods and any associated references are available in the online version of the paper at http://www.nature.com/naturemedicine/.

Note: Supplementary information is available on the Nature Medicine website.

AUTHOR CONTRIBUTIONS
J.N.W. came up with the hypothesis, designed and performed the experiments, analyzed the data and wrote the manuscript. J.B. and M.A.M. designed and performed the experiments and analyzed the data. K.U. came up with the hypothesis and generated reagents. C.R.K. came up with the hypothesis, helped analyze the data and wrote the manuscript.

1. Gotto, A.M. Jr. et al. The metabolic syndrome: a call to action. Coron. Artery Dis. 17, 77–80 (2006).
2. Ford, E.S., Giles, W.H. & Mokdad, A.H. Increasing prevalence of the metabolic syndrome among US adults. Diabetes Care 27, 2444–2449 (2004).
3. Dandona, P., Aljada, A. & Bandyopadhyay, A. Inflammation: the link between insulin resistance, obesity and diabetes. Trends Immunol. 25, 4–7 (2004).
4. Hotamisligil, G.S. Inflammation and metabolic disorders. Nature 444, 860–867 (2006).

5. Vanhaesebroeck, B., Stein, R.C. & Waterfield, M.D. The study of phosphoinositide 3-kinase function. *Cancer Surv.* **27**, 249–270 (1996).
6. Cheatham, B. *et al.* Phosphatidylinositol 3-kinase activation is required for insulin stimulation of pp70 S6 kinase, DNA synthesis and glucose transporter translocation. *Mol. Cell. Biol.* **14**, 4902–4911 (1994).
7. Sharma, P.M. *et al.* Inhibition of phosphatidylinositol 3-kinase activity by adenovirus-mediated gene transfer and its effect on insulin action. *J. Biol. Chem.* [In Process Citation] **273**, 18528–18537 (1998).
8. Cusi, K. *et al.* Insulin resistance differentially affects the PI 3-kinase– and MAP kinase–mediated signaling in human muscle. *J. Clin. Invest.* **105**, 311–320 (2000).
9. Heydrick, S.J., Gautier, N., Olichon-Berthe, C., Van Obberghen, E. & Le Marchand-Brustel, Y Early alteration of insulin stimulation of PI 3-kinase in muscle and adipocyte from gold thioglucose obese mice. *Am. J. Physiol.* **268**, E604–E612 (1995).
10. Bandyopadhyay, G.K., Yu, J.G., Ofrecio, J. & Olefsky, J.M. Increased p85/55/50 expression and decreased phosphotidylinositol 3-kinase activity in insulin-resistant human skeletal muscle. *Diabetes* **54**, 2351–2359 (2005).
11. Ni, M. & Lee, A.S. ER chaperones in mammalian development and human diseases. *FEBS Lett.* **581**, 3641–3651 (2007).
12. Dobson, C.M. Principles of protein folding, misfolding and aggregation. *Semin. Cell Dev. Biol.* **15**, 3–16 (2004).
13. Schröder, M. & Kaufman, R. ER stress and the unfolded protein response. *Mutat. Res.* **569**, 29–63 (2005).
14. Ron, D. & Walter, P. Signal integration in the endoplasmic reticulum unfolded protein response. *Nat. Rev. Mol. Cell Biol.* **8**, 519–529 (2007).
15. Elouil, H. *et al.* Acute nutrient regulation of the unfolded protein response and integrated stress response in cultured rat pancreatic islets. *Diabetologia* **50**, 1442–1452 (2007).
16. Lee, A.S. Mammalian stress response: induction of the glucose-regulated protein family. *Curr. Opin. Cell Biol.* **4**, 267–273 (1992).
17. He, B. Viruses, endoplasmic reticulum stress and interferon responses. *Cell Death Differ.* **13**, 393–403 (2006).
18. Boden, G. *et al.* Increase in endoplasmic reticulum stress-related proteins and genes in adipose tissue of obese, insulin-resistant individuals. *Diabetes* **57**, 2438–2444 (2008).
19. Ozcan, U. *et al.* Endoplasmic reticulum stress links obesity, insulin action, and type 2 diabetes. *Science* **306**, 457–461 (2004).
20. Eizirik, D.L., Cardozo, A.K. & Cnop, M. The role for endoplasmic reticulum stress in diabetes mellitus. *Endocr. Rev.* **29**, 42–61 (2008).
21. Gregor, M.F. *et al.* Endoplasmic reticulum stress is reduced in tissues of obese subjects after weight loss. *Diabetes* **58**, 693–700 (2009).
22. Ozawa, K. *et al.* The endoplasmic reticulum chaperone improves insulin resistance in type 2 diabetes. *Diabetes* **54**, 657–663 (2005).
23. Ozcan, U. *et al.* Chemical chaperones reduce ER stress and restore glucose homeostasis in a mouse model of type 2 diabetes. *Science* **313**, 1137–1140 (2006).
24. Tanti, J.F. *et al.* Alteration in insulin action: role of IRS-1 serine phosphorylation in the retroregulation of insulin signalling. *Ann. Endocrinol. (Paris)* **65**, 43–48 (2004).
25. Gao, Z. *et al.* Inhibition of insulin sensitivity by free fatty acids requires activation of multiple serine kinases in 3T3-L1 adipocytes. *Mol. Endocrinol.* **18**, 2024–2034 (2004).
26. Herschkovitz, A. *et al.* Common inhibitory serine sites phosphorylated by IRS-1 kinases, triggered by insulin and inducers of insulin resistance. *J. Biol. Chem.* **282**, 18018–18027 (2007).
27. Yoshida, H., Matsui, T., Yamamoto, A., Okada, T. & Mori, K. XBP1 mRNA is induced by ATF6 and spliced by IRE1 in response to ER stress to produce a highly active transcription factor. *Cell* **107**, 881–891 (2001).
28. Ron, D. & Hubbard, S.R. How IRE1 reacts to ER stress. *Cell* **132**, 24–26 (2008).
29. Ueki, K. *et al.* Positive and negative roles of p85α and p85β regulatory subunits of phosphoinositide 3-kinase in insulin signaling. *J. Biol. Chem.* **278**, 48453–48466 (2003).
30. Terauchi, Y. *et al.* Increased insulin sensitivity and hypoglycaemia in mice lacking the p85α subunit of phosphoinositide 3-kinase. *Nat. Genet.* **21**, 230–235 (1999).
31. Taniguchi, C.M. *et al.* The p85α regulatory subunit of phosphoinositide 3-kinase potentiates c-Jun N-terminal kinase–mediated insulin resistance. *Mol. Cell. Biol.* **27**, 2830–2840 (2007).
32. Forler, D. *et al.* An efficient protein complex purification method for functional proteomics in higher eukaryotes. *Nat. Biotechnol.* **21**, 89–92 (2003).
33. Rigaut, G. *et al.* A generic protein purification method for protein complex characterization and proteome exploration. *Nat. Biotechnol.* **17**, 1030–1032 (1999).
34. Tirosh, B., Iwakoshi, N.N., Glimcher, L.H. & Ploegh, H.L. Rapid turnover of unspliced Xbp-1 as a factor that modulates the unfolded protein response. *J. Biol. Chem.* **281**, 5852–5860 (2006).
35. Yoshida, H., Oku, M., Suzuki, M. & Mori, K. pXBP1$_U$ encoded in XBP1 pre-mRNA negatively regulates unfolded protein response activator pXBP1$_S$ in mammalian ER stress response. *J. Cell Biol.* **172**, 565–575 (2006).
36. Fonseca, S.G., Lipson, K.L. & Urano, F. Endoplasmic reticulum stress signaling in pancreatic beta-cells. *Antioxid. Redox Signal.* **9**, 2335–2344 (2007).
37. Harding, H.P. & Ron, D. Endoplasmic reticulum stress and the development of diabetes: a review. *Diabetes* **51** Suppl 3, S455–S461 (2002).
38. Eizirik, D.L., Cardozo, A.K. & Cnop, M. The role for endoplasmic reticulum stress in diabetes mellitus. *Endocr. Rev.* **29**, 42–61 (2008).
39. Nakatani, Y. *et al.* Involvement of endoplasmic reticulum stress in insulin resistance and diabetes. *J. Biol. Chem.* **280**, 847–851 (2005).
40. Shoelson, S.E., Lee, J. & Goldfine, A.B. Inflammation and insulin resistance. *J. Clin. Invest.* **116**, 1793–1801 (2006).
41. Shepherd, P.R., Withers, D.J. & Siddle, K. Phosphoinositide 3-kinase: the key switch mechanism in insulin signalling. *Biochem. J.* **333**, 471–490 (1998).
42. Duronio, V., Scheid, M.P. & Ettinger, S. Downstream signalling events regulated by phosphatidylinositol 3-kinase activity. *Cell. Signal.* **10**, 233–239 (1998).
43. Barbour, L.A. *et al.* Human placental growth hormone increases expression of the p85 regulatory unit of phosphatidylinositol 3-kinase and triggers severe insulin resistance in skeletal muscle. *Endocrinology* **145**, 1144–1150 (2004).
44. Khalfallah, Y., Sassolas, G., Borson-Chazot, F., Vega, N. & Vidal, H. Expression of insulin target genes in skeletal muscle and adipose tissue in adult patients with growth hormone deficiency: effect of one year recombinant human growth hormone therapy. *J. Endocrinol.* **171**, 285–292 (2001).
45. Barbour, L.A. *et al.* Human placental growth hormone increases expression of the p85 regulatory unit of phosphatidylinositol 3-kinase and triggers severe insulin resistance in skeletal muscle. *Endocrinology* **145**, 1144–1150 (2004).
46. Luo, J. & Cantley, L.C. The negative regulation of phosphoinositide 3-kinase signaling by p85 and it's implication in cancer. *Cell Cycle* **4**, 1309–1312 (2005).
47. Yeates, L.C., Gallegos, A., Kozikowski, A.P. & Powis, G. Down regulation of the expression of the p110, p85 and p55 subunits of phosphatidylinositol 3-kinase during colon cancer cell anchorage-independent growth. *Anticancer Res.* **19**, 4171–4176 (1999).
48. Fang, D. & Liu, Y.C. Proteolysis-independent regulation of PI3K by Cbl-b–mediated ubiquitination in T cells. *Nat. Immunol.* **2**, 870–875 (2001).
49. García, Z. *et al.* A PI3K activity–independent function of p85 regulatory subunit in control of mammalian cytokinesis. *EMBO J.* **25**, 4740–4751 (2006).
50. Park, S.W., Zhou, Y., Lee, J., Lu, A., Sun, C., Chung, J., Ueki, K. & Ozcan, U. Regulatory subunits of PI3K, p85α and p85β, interact with XBP1 and increase its nuclear translocation. *Nat. Med.* advance online publication, doi:10.1038/nm.2099 (28 March 2010).
51. Yamamoto, K. *et al.* Transcriptional induction of mammalian ER quality control proteins is mediated by single or combined action of ATF6α and XBP1. *Dev. Cell* **13**, 365–376 (2007).
52. Mauvais-Jarvis, F. *et al.* Reduced expression of the murine p85α subunit of phosphoinositide 3-kinase improves insulin signaling and ameliorates diabetes. *J. Clin. Invest.* **109**, 141–149 (2002).
53. Chen, D. *et al.* p50α/p55α phosphoinositide 3-kinase knockout mice exhibit enhanced insulin sensitivity. *Mol. Cell. Biol.* **24**, 320–329 (2004).
54. Brachmann, S.M., Ueki, K., Engelman, J.A., Kahn, R.C. & Cantley, L.C. Phosphoinositide 3-kinase catalytic subunit deletion and regulatory subunit deletion have opposite effects on insulin sensitivity in mice. *Mol. Cell. Biol.* **25**, 1596–1607 (2005).
55. Wellen, K.E. & Hotamisligil, G.S. Inflammation, stress, and diabetes. *J. Clin. Invest.* **115**, 1111–1119 (2005).
56. Hotamisligil, G.S. Inflammation and metabolic disorders. *Nature* **444**, 860–867 (2006).
57. Kerouz, N.J., Hörsch, D., Pons, S. & Kahn, C.R. Differential regulation of insulin receptor substrates-1 and -2 (IRS-1 and IRS-2) and phosphatidylinositol 3-kinase isoforms in liver and muscle of the obese diabetic (ob/ob) mouse. *J. Clin. Invest.* **100**, 3164–3172 (1997).
58. Calfon, M. *et al.* IRE1 couples endoplasmic reticulum load to secretory capacity by processing the *XBP-1* mRNA. *Nature* **415**, 92–96 (2002).

- 566 -

ONLINE METHODS

Chemicals and materials. We purchased tunicamycin, protease inhibitor cocktail (4-(2-aminoethyl) benzenesulfonyl fluoride hydrochloride, pepstatin A, E-64, bestatin, leupeptin and aprotinin) and streptavidin agarose from Sigma-Aldrich. We purchased thapsigargin from Santa Cruz Biotechnology.

Antibodies. We obtained rabbit antibodies specific for BiP (3177), phospho-PERK (3179), calnexin (2433), IRE1α (3294), PDI (2466), Grp94 (2104) and PERK (3192) from Cell Signaling Technologies and calreticulin (ab2907) from Abcam. We purchased rabbit polyclonal antibody to phospho-IRE1α (Ser724) from Novus Biologicals (NB100-2323) and rabbit polyclonal antibody XBP-1 (M-186) from Santa Cruz. We purchased monoclonal antibody to ATF6 from Santa Cruz (H-280) and monoclonal antibody to Flag (M2) from Sigma-Aldrich. Horseradish peroxidase–conjugated antibody to actin was from Santa Cruz Biotechnology (I-19).

Bacterial two-hybrid screen. To screen for interacting partners that specifically associate with the N-terminal portion of p85α, we cloned the nucleotide sequence corresponding to amino acids 2–202 into the pBT vector (Stratagene) to generate a fusion of the bacteriophage λ repressor protein. We screened a human liver BacterioMatch two-hybrid cDNA library in the pTRG plasmid (Stratagene) with the constructed pBT-NH2-p85α using the manufacturer's protocols.

Mammalian tissue culture, transfection and sample preparation. We cultured mouse brown preadipocytes, Huh7 hepatoma cells and human embryonic kidney 293T (HEK 293T) cells at 37 °C and 5% CO_2 and maintained them in DMEM supplemented with streptomycin-penicillin and 10% FBS. We cultured the FAO rat hepatoma cell line under identical conditions in Coon's modified Ham's F12 medium supplemented with streptomycin-penicillin and 10% FBS. We performed transient transfections on HEK 293T cells at 80% confluence with Transit-Express as outlined by the manufacturer (Mirus). After treatment, we washed the cells two times in ice-cold PBS (pH 7.4), collected by centrifugation at 660g for 5 min and resuspended them in lysis buffer (50 mM Tris-HCl pH 7.4, 150 mM NaCl, 2 mM EDTA, 1% NP-40, 0.1% SDS and 0.1% Triton X-100) supplemented with protease inhibitors. We spun cell extracts at 20,800g for 10 min at 4 °C to remove insoluble material.

Immunoprecipitation and streptavidin precipitation. We performed immunoprecipitations on whole-cell lysates prepared as previously described[59]. We diluted cleared lysates tenfold in immunoprecipitation buffer (10 mM HEPES pH 7.9, 100 mM NaCl, 5% glycerol, 0.5% NP-40, 0.1 mM EGTA, 0.1 mM EDTA, 1 mM dithiothreitol and 10 mM β-glycerophosphate and 10 mM NaF) supplemented with protease inhibitors. After 2 h of incubation with HA-conjugated agarose, we washed immunoprecipitates three times with immunoprecipitation buffer and resuspended them in Laemmli sample buffer before resolution by SDS-PAGE, transfer to polyvinylidene fluoride and immunoblotting. We performed streptavidin precipitations by the same protocol with the exception that we used streptavidin-conjugated agarose to precipitate p85α fused to a tandem affinity purification (TAP) epitope tag.

Analysis of gene expression by quantitative reverse transcription-PCR. We purified total RNA with the RNeasy mini kit (Qiagen) with the inclusion of an on-column DNase digestion. We reverse-transcribed 2 µg of total RNA with the High-Capacity cDNA Reverse Transcription Kit (Applied Biosystems). We amplified a portion of diluted cDNA with specific primers with a SYBR green PCR master mix (Applied Biosystems) on an ABI Prism 7500HT instrument. For each gene, we determined mRNA expression relative to TATA-binding protein as an internal control. We assessed the assay fidelity for each primer pair by performing melting-curve analysis. The nucleotide sequences of primers used for quantitative PCR are available upon request.

Recombinant adenovirus. We purchased the control GFP adenovirus from CellBioLabs. To create the TAP-p85α recombinant adenovirus, we ligated the full-length cDNA of human p85α into pNTAP and adenovirus produced according to the AdEasy (Stratgene) protocol.

Analysis of apoptosis. We incubated cells with growth medium alone or medium containing 2 µM tunicamycin or 100 µg ml^{-1} thapsigargin for 24 h. At the end of the incubation period, we collected medium containing floating cells. We rinsed the cells with PBS, which we then added to the medium containing the floating cells. We resuspended the attached cells with trypsin and pooled them with the floating cells. We collected the cells by centrifugation, washed them once in PBS and then resuspended them in 400 µl of binding buffer (0.1 M HEPES, pH 7.4, 1.4 M NaCl, 25 mM $CaCl_2$). We then incubated the cells with 5 µl annexin V coupled to PE (BD Biosciences) and 2.5 µg ml^{-1} propidium iodide for 15 min at 22 °C and submitted them for FACS analysis.

Mice. We housed all mice on a 12-h light-dark cycle and fed them a standard rodent chow. All protocols for mouse use, tunicamycin administration and killing were approved by the Animal Care Use Committee of the Joslin Diabetes Center and Harvard Medical School in accordance with US National Institutes of Health guidelines. All mice used in the study were on a 129Sv-C57BL/6 mixed genetic background. We administered tunicamycin by intraperitoneal injection at a final dose of 2.5 µg per g body weight in a 150 mM glucose solution in saline as previously described[60]. We gave control mice 150 mM glucose in saline by intraperitoneal injection.

Liver immunoblot analysis. We prepared liver protein in a tissue homogenization buffer (25 mM Tris-HCl, (pH 7.4), 10 mM Na_3VO_4, 100 mM NaF, 50 mM $Na_4P_2O_7$, 10 mM EGTA, 10 mM EDTA, 1% NP-40 and 0.1% SDS) supplemented with protease inhibitors. We cleared insoluble protein by centrifugation at 55,000 r.p.m. in a 70.1TI rotor (Beckman) and determined the protein concentrations of cleared lysates by the Bradford method. We quantified all protein expression data by densitometry with US National Institutes of Health ImageJ software.

Statistics. Data are presented as means ± s.e.m. We used a two-tailed Student's t test for statistical analysis between two groups.

59. Brüning, J.C., Winnay, J., Cheatham, B. & Kahn, C.R. *Mol. Cell Biol.* **17**, 1513–1521 (1997).
60. Marciniak, S.J. *et al.* CHOP induces death by promoting protein synthesis and oxidation in the stressed endoplasmic reticulum. *Genes Dev.* **18**, 3066–3077 (2004).

A Novel Interaction Between the Regulatory Subunit of PI 3-Kinase and X-box Binding Protein-1 Modulates the Unfolded Protein Response

Jonathon N. Winnay [1], Jeremie Boucher [1*], Marcelo Mori [1*], Kohjiro Ueki [2] and C. Ronald Kahn [1]

S1
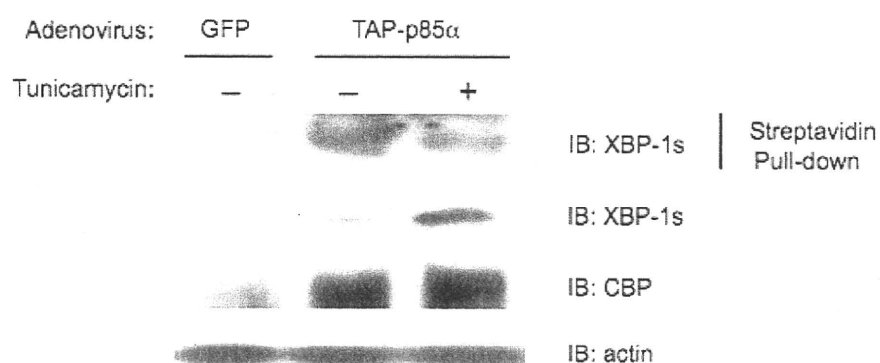
Supplemental Figure 1: XBP-1s interacts with p85 in an ER-stress dependent manner. Crude lysate containing recombinant adenovirus expressing GFP or TAP-p85α were used to infect FAO cells. Two days later, cells were treated with vehicle (DMSO) or tunicamycin (2 µg ml⁻¹) for 5 hours. Streptavidin resin was used to precipitate TAP-p85α, samples resolved by SDS-PAGE and immunoblots performed with XBP-1s antibodies. Anti-actin immunoblots were performed to confirm equal protein was added for each condition.
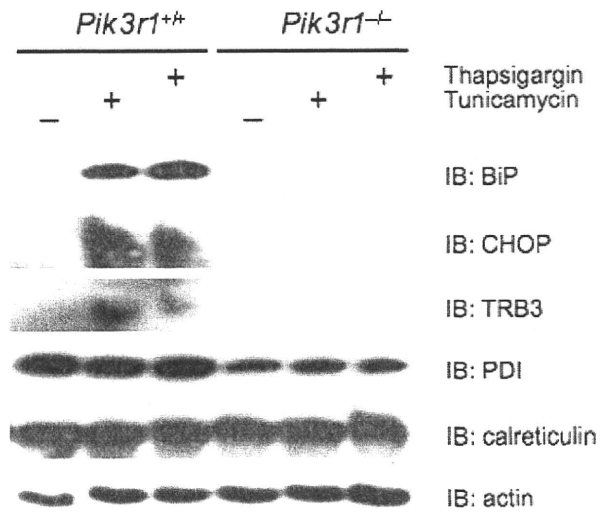
Supplemental Figure 2: A blunted UPR is observed in p85α-deficient cells following induction of ER stress. Control and p85α-deficient fibroblasts were treated with vehicle (DMSO), 2 µg ml⁻¹ Tunicamycin or 100 nm Thapsigargin for five hours. Whole cell lysates were immunoblotted with the indicated antibodies. Immunoblots performed with anti-actin antibodies confirmed equal protein loading.
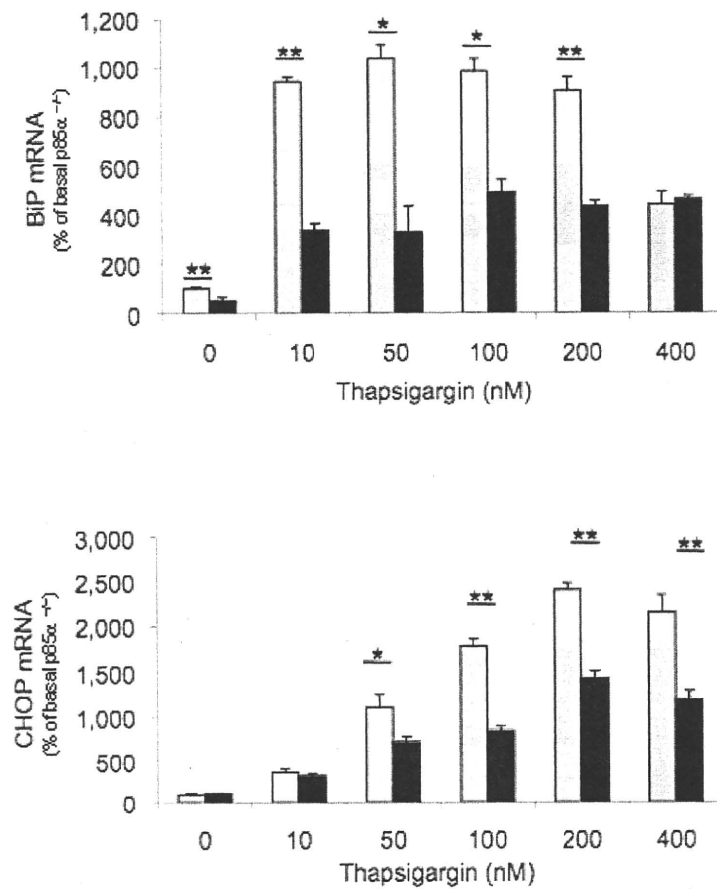
Supplemental Figure 3: Dose-response of UPR target-gene expression. Quantitative RT-PCR was performed on cDNA derived from control and Pik3r1$^{-/-}$ cells treated with the indicated concentrations of thapsigargin for five hours. Data were normalized using TBP as an internal reference.
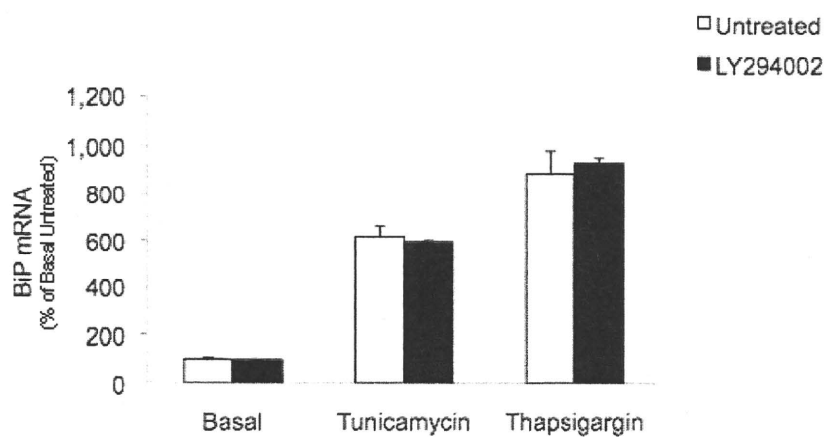
Supplemental Figure 4: Effect of PI 3-kinase inhibition on UPR target-gene expression. Quantitative RT-PCR was performed on cDNA derived from control and *Pik3r1−/−* cells treated with tunicamycin (2 µg ml^{-1}) or thapsigargin (100 nM) for five hours in the absence or presence of LY294002 (50 µM).